



# Breakdown Pressure and Propagation Surface of a Hydraulically Pressurized Circular Notch Within a Rock Material

Adam K. Schwartzkopff<sup>1,2</sup> · Nouné S. Melkougian<sup>1</sup> · Chaoshui Xu<sup>1,3</sup>

Received: 8 November 2018 / Accepted: 26 September 2020 / Published online: 12 October 2020  
© Springer-Verlag GmbH Austria, part of Springer Nature 2020

## Abstract

Rock masses contain pre-existing cracks. These cracks are not usually considered when predicting the maximum injection pressure, i.e. the breakdown pressure, in hydraulic fracture stimulations. The conventional approach to predict breakdown pressure is to use the maximum tensile stress failure criterion to calculate the pressure when a point on the borehole wall reaches the tensile strength of the rock. In addition, a pre-existing crack intersecting a hydraulically pressurized section of a borehole may produce a non-planar crack propagation surface. It is important to predict these non-planar crack propagation surfaces to design productive hydraulic fracturing stimulations and to mitigate risks associated with uncertainties of the resultant crack propagation. To gain a better understanding of this problem, a series of hydraulic fracturing experiments were conducted to investigate the breakdown pressures and crack propagation surfaces of a pressurized circular crack represented by a thin notch, subjected to different external triaxial stresses. The results show that the breakdown pressures under the shear stress conditions studied can be estimated using only the resultant normal stress on the plane of the crack. As the material properties of the experimental specimens are well defined and the crack propagation surfaces were mapped, the experimental results presented in this study provide a very useful measured dataset for the validation of various modelling approaches. The propagation surfaces from experiments were found to align closely to the computational predictions based on the maximum tangential stress criterion. Finally, this study gives evidence in three-dimensions that via the hydraulic fracturing process, the propagation of an initially arbitrarily oriented crack will eventually realign to be perpendicular to the minor principal stress direction.

**Keywords** Hydraulic fracturing · Fracture mechanics · Three-dimensional crack propagation · Breakdown pressure · Pre-existing cracks

## Abbreviations

CCNBD	Cracked chevron notched Brazilian disc
LEFM	Linear elastic fracture mechanics

## List of symbols

$a$	Radius or major axis of the elliptical crack (m)
$a_{\text{median}}$	Median crack increment input for FRANC3D (m)
$inc$	Predefined incremental length for the proposed analytical method (m)
$inc_{\text{FRANC3D}}(\varphi)$	Incremental length used in FRANC3D (m)
$K_{\text{I}(\text{median})}$	Median stress intensity factor for Mode I along the crack front ( $\text{Pa}\sqrt{\text{m}}$ )
$K_{\text{I}}(\varphi)$	Mode I stress intensity factor ( $\text{Pa}\sqrt{\text{m}}$ )
$K_{\text{II}}(\varphi)$	Mode II stress intensity factor ( $\text{Pa}\sqrt{\text{m}}$ )
$K_{\text{III}}(\varphi)$	Mode III stress intensity factor ( $\text{Pa}\sqrt{\text{m}}$ )
$K_{\text{Ic}}$	Fracture toughness for Mode I ( $\text{Pa}\sqrt{\text{m}}$ )
$n$	Power input for calculating the incremental length in FRANC3D

✉ Adam K. Schwartzkopff  
aschwartzkopff@kumamoto-u.ac.jp

Nouné S. Melkougian  
noune.melkougian@adelaide.edu.au

Chaoshui Xu  
chaoshui.xu@adelaide.edu.au

<sup>1</sup> School of Civil, Environmental and Mining Engineering, Faculty of Engineering, Computer and Mathematical Sciences, The University of Adelaide, Adelaide, SA 5005, Australia

<sup>2</sup> International Research Organization for Advanced Science and Technology, Kumamoto University, Kumamoto, Kumamoto Prefecture 860-8555, Japan

<sup>3</sup> School of Resource and Environmental Engineering, Wuhan University of Science and Technology, Wuhan, China

**Greek letters**

$\alpha$	Dip direction (°)
$\beta$	Dip angle (°)
$\theta$	Crack front angle—from the normal to the crack front towards the positive $z$ axis direction (°)
$\theta_c$ ( $\varphi$ )	Critical crack front angle (°)
$\mu$	Friction coefficient
$\nu$	Poisson's ratio
$\sigma_n'$	Effective normal stress on the surface of the crack (Pa)
$\sigma_{n(\text{external})}$	Normal stress on the surface of the crack (Pa)
$\tau$	Shear stress along the surface of the crack (Pa)
$\tau_{\text{net}}$	Net shear stress along the surface of the crack (Pa)
$\varphi$	Crack front angle—from the $x$ axis direction clockwise around the normal vector in the positive $z$ axis direction (°)
$\omega$	Shear angle— clockwise around the normal vector in the positive $z$ axis direction (°)

**1 Introduction**

It is important to be able to predict the crack propagation surfaces resulting from hydraulic fracturing since these cracks produce the primary flow pathways for hydrocarbon extraction in oil and gas engineering and the heat exchange areas for geothermal energy exploitation. The pre-existing and induced crack surfaces from hydraulic fracturing will also change reservoir permeability by connecting cracks and voids in the rock. The stress field near a pre-existing crack is determined by the in-situ stress conditions and the internal fluid pressure of the propagating crack. Together, these factors control the shape of the crack propagation surface resulting from hydraulic fracturing. This process normally produces crack propagation surfaces that are perpendicular to the minor principal stress direction, but existing discontinuities in the rock mass increase the complexity of the crack propagation. In geothermal energy extraction, resultant cracks from hydraulic stimulations are normally the major fluid conduits to connect injection and extraction wells if the initial permeability of the rock mass is too low to allow fluid circulation. It is, therefore, important to understand the shape and orientation of resultant cracks generated by hydraulic stimulations to better design the productive operations and to mitigate risks associated with uncertainties due to the propagation of the resultant cracks.

A review of available literature indicates that whilst there are numerical models developed to predict crack propagation surfaces for rocks that have pre-existing cracks, there are very few experimental benchmark results to validate these models. To this end, this study includes hydraulic fracturing experiments that consider the influence of a pre-existing pressurized circular crack (Fig. 1a) represented by a thin notch intersecting a pressurized borehole section, on the crack propagation surface produced. The experimental results were then used to validate a model developed by the authors as described in Schwartzkopff et al. (2016).

Hydraulic fracturing experiments using intact rocks have shown that the crack propagation surface produced is perpendicular to the minor principal stress direction, e.g. Hubbert and Willis (1957). The same process is assumed to govern the hydraulic crack propagation in a discontinuous rock mass, whereby the propagation surface will eventually realign to be perpendicular to the minor principal stress direction, but through a much more complex tortuous propagation process.

Pre-existing cracks intersecting the pressurized borehole section (e.g., Fig. 1a) in hydraulic fracturing influence the initial pressures and the resultant crack propagation surface. Zoback et al. (1977) conducted one of the first investigations into the influence of a pre-existing crack using hydraulic fracturing, where the pre-existing crack was perpendicular to the direction of the only applied stress, i.e. major external principal stress, and there were no other external stresses applied in their experiments. Using this pre-existing crack orientation, they were not able to study the reorientation process, since a new crack was produced parallel to the direction of the major external principal stress. If the pre-existing crack is aligned in a principal stress direction then there is no Mode II (in plane shear stress component) loading, since there is no net shear stress on the surface of the pre-existing crack. Under pure Mode I (tensile opening) the crack propagates in the same plane (Erdogan and Sih 1963). Yan et al. (2011) assessed the influence of the pre-existing weaknesses on hydraulic fracturing by placing an A4 piece of paper into four concrete specimens. Two of these specimens had the paper intersecting the borehole to study the influence of a pre-existing weakness on the resultant crack propagation surface. They did not map and digitize the propagation surfaces, although they did conclude that the crack propagated in the direction of the pre-existing weakness and gradually reoriented to be perpendicular to the minor principal stress direction. Clearly, there is a need to map these propagation surfaces since this will provide a very useful quantitative database for validation of numerical models in future research, as opposed to published photos, which only give a qualitative description of these surfaces. The two above mentioned studies further suggest the need for a detailed investigation into the breakdown pressures and

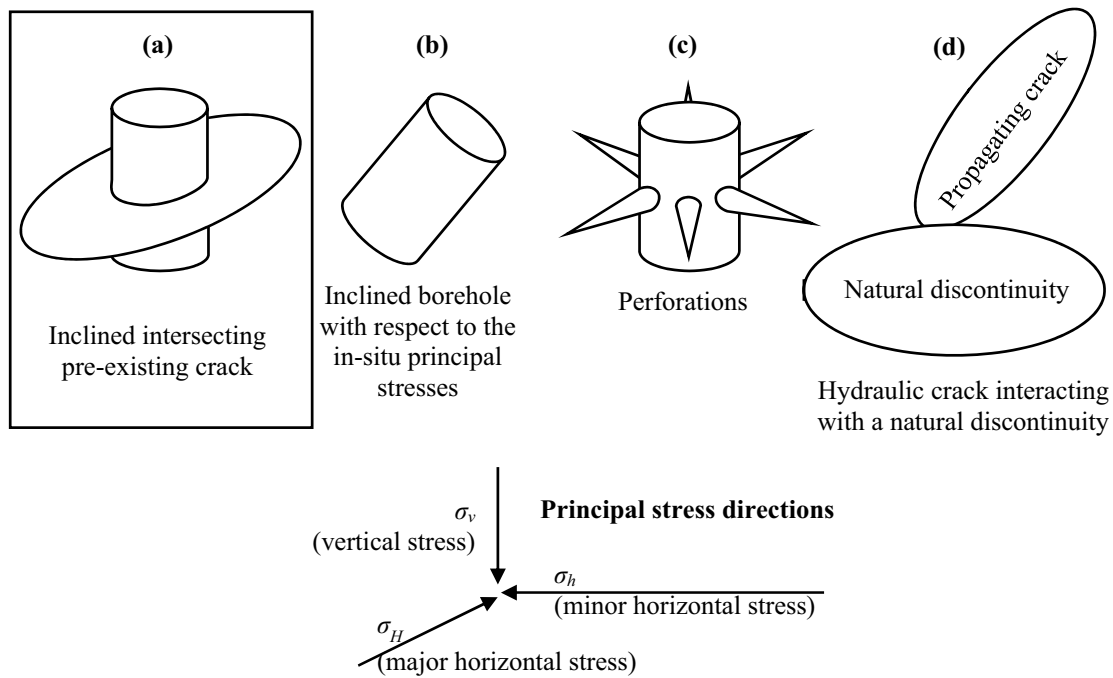


**Fig. 1** Different scenarios where the propagating crack can reorient during hydraulic fracturing: **a** an inclined crack intersecting the pressurized borehole section (the scenario that is considered in this study), **b** a pressurized borehole inclined with respect to the in-situ

compressive principal remote stresses, **c** a pressurized borehole that has perforations around its circumference, and **d** a propagating pressurized crack interacting with natural discontinuities

propagation surfaces from inclined pre-existing notches in rock-like material.

Other published studies have dealt with non-planar propagations of hydraulic fracturing near a pressurized borehole section (Abass et al. 1996; Daneshy 1973; Fallahzadeh et al. 2015; Zhang and Chen 2010). Abass et al. (1996) and Daneshy (1973) both used a borehole that was orientated at an angle to the direction of a principal remote compressive stress (Fig. 1b) to induce a non-planar crack propagation from hydraulic fracturing. However, these studies are not the same experimental setup as was used in the study presented in this paper, since a pre-existing crack intersecting the borehole was not introduced into their specimens. Zhang and Chen (2010) studied the role of a perforation orientation on the resultant crack propagation surface by controlling the initial crack orientation in intact rock. The perforation orientation was controlled by directing the pressured fluid through an orifice. No pre-existing cracks were introduced in their specimens either, although the perforation orientation did produce an initial crack orientation that was not perpendicular to the minor principal stress, though the induced crack eventually reoriented to be approximately perpendicular to the minor principal stress direction. Fallahzadeh et al. (2015) studied the crack propagation reorientation from four and one perforations (perpendicular to the injection borehole axis). Note, these perforations are different from pre-existing

natural discontinuities or the ones created artificially in this study, since they are generated with a perforation gun, which creates an intruding long and thin damaged zone from the injection borehole within the rock. Figure 1c illustrates these damaged zones that are usually approximately perpendicular to the borehole axis. Fallahzadeh et al. (2015) provided the initiation and breakdown pressure of their experiments but they did not use any model to predict these values.

In summary, all these published studies are considered to be different from the current investigation. The non-planar crack propagation studied in these works occurred due to either an inclined borehole with respect to one of the principal stress directions or different perforation direction, which is different to the geometrical configuration of an inclined pre-existing discontinuity intersecting a borehole studied in this work, a case commonly observed in practice.

In this study, the height of the pressurized borehole section is insignificant compared with the borehole radius. Hence, the borehole geometry is assumed to have little to no influence on the breakdown pressure of the initial notch and the resultant crack propagation surface. In other words, this study does not address the problem of a pressurized borehole section containing a notch in which the section is long compared with the borehole radius (Abbas and Lecampion 2013; Detournay and Carbonell 1997; Lhomme et al. 2005; Weijers 1995). There are other published studies dealing

with the interaction of an initially planar hydraulic crack with a natural discontinuity, see Fig. 1d (Fu et al. 2016; Llanos et al. 2017; Renshaw and Pollard 1995; Sarmadivaleh 2012; Warpinski and Teufel 1987; Zhou et al. 2008). However, these studies focus on the interaction of a discontinuity away from the borehole. Pre-existing cracks not intersecting the borehole can also affect the shape and orientation of the crack propagation surface within the rock mass, but this aspect is not addressed in this study. Note from the perspective of borehole pressurization, there is no significant difference between a natural and an induced discontinuity intersecting the pressurized borehole section. The simplified geometry of a circular crack was used in this study to make easier comparisons between experiments and numerical models. A crack intersecting a borehole will be pressurized and propagate from the crack front. When a crack propagation front interacts with a natural discontinuity, the interaction can be complex, i.e. the propagating crack can arrest, divert, penetrate or offset near the discontinuity (Khoei et al. 2018). Figure 1 shows different scenarios that a propagating crack can reorient during the hydraulic fracturing process.

The experiments conducted in this study are mapped to provide a set of digitized propagation surfaces for the reorientation process of an inclined circular crack intersecting a borehole. The experimental crack propagation surfaces presented in this study provide a useful measured dataset for the validation of various modelling approaches. As an example, the results were used to validate the numerical modelling undertaken in this study, which illustrates the capability of linear elastic fracture mechanics (LEFM) for the prediction of three-dimensional crack propagation surfaces. The first propagation front was calculated using stress intensity factors from the analytical solution based on the initial configuration. Subsequent stress intensity factors and crack propagation surface predictions were calculated using a finite element method (FEM) code. The validation included comparisons of the experimental and modelled crack propagation surfaces and regression analyses along cross-sections. This contributes to the understanding of the reorientation

process of a pre-existing crack intersecting with a borehole section during hydraulic fracturing.

## 2 Material Properties and Hydraulic Fracturing Experimental Methods

The detailed experimental method is presented in this section. The properties of the material used in the hydraulic fracturing experiments are reported, and the procedure for the hydraulic fracturing experiments is described below.

### 2.1 Material and Specimen Preparation

The material used in this study was chosen so that it is homogeneous, isotropic and brittle. Hence, a high strength concrete with properties similar to granite was used. Rocks subjected to hydraulic fracturing treatments, in general, are of low permeability (Caineng et al. 2010; Fridleifsson and Freeston 1994; Majer et al. 2007; Zimmermann and Reinicke 2010). For example, engineered geothermal systems are generally located in granite basements (Häring et al. 2008; Majer et al. 2007; Xu et al. 2015), whereas unconventional gas reservoirs are in general located in shales or mudstones (Rogner 1997).

The ranges of reported properties of granite obtained from the literature (Arzúa and Alejano 2013; Backers et al. 2002; Bell 2013; Nasserri and Mohanty 2008; Stimpson 1970; Xu 2010; Yesiloglu-Gultekin et al. 2013) are listed in Table 1. These values were used as a guide to formulate the required mechanical properties of the artificial rock (concrete) used in this work, which are listed in Table 3.

A prototype specimen was created using the material mass ratios reported in Table 2. Part of the mould was created from acrylonitrile butadiene styrene (ABS) using a three-dimensional printer. A plastic cylinder was placed around the part created in the three-dimensional printer to create a central cavity into which the high strength concrete mixture was poured (see Fig. 2).

**Table 1** Range of granite mechanical properties used for assessment of the artificial rock (concrete) employed in this study

Material characteristic	Minimum reported value	Maximum reported value	Minimum number of values	References
Elastic modulus (GPa)	18	48	6	Arzúa and Alejano (2013), Backers et al. (2002) and Stimpson (1970)
Poisson's ratio	0.16	0.19	4	Arzúa and Alejano (2013) and Backers et al. (2002)
Uniaxial compressive strength (MPa)	64	321	124	Arzúa and Alejano (2013), Bell (2013) and Yesiloglu-Gultekin et al. (2013)
Mode I fracture toughness (MPa $\sqrt{\text{m}}$ )	0.71	2.20	74	Nasserri and Mohanty (2008) and Xu (2010)
Tensile strength (MPa)	5.1	16.4	78	Arzúa and Alejano (2013) and Yesiloglu-Gultekin et al. (2013)

**Table 2** Materials and mass values used for the artificial rock mixture

Materials	Mass ratios
Sulphate resisting cement	1
Sand 60G	0.5
Sand 30/60	0.5
Silica fume	0.27
Water	0.17
Super plasticizer (ViscoCrete®10)	0.06
Total	2.50

The same procedure was followed for all specimens, as stated below. Once the specimen was cured (after 28 days in the fog room), the centre plastic cylinder was drilled out, using a 6.30 mm diameter drill bit, to create a borehole in the specimen. The plastic disc inside the body was then removed by submerging the cured material into a vessel filled with acetone for approximately 4 weeks (28 days). All plastics were removed successfully using this process to create the desired borehole and the circular notch, to represent a crack, at the bottom of the borehole, as shown in Fig. 3.

The designed specimen geometry is shown in Fig. 4. The geometry was chosen so that the specimen had the largest possible diameter to fit in a Hoek cell. This diameter was approximately 63.5 mm and, therefore, the length had to be approximately 127 mm to fit into this apparatus. Large specimen size will help reduce the boundary effect on the breakdown pressure. In addition, this specimen size allows for greater crack propagation area within the artificial rock. The circular groove (or indent) was designed

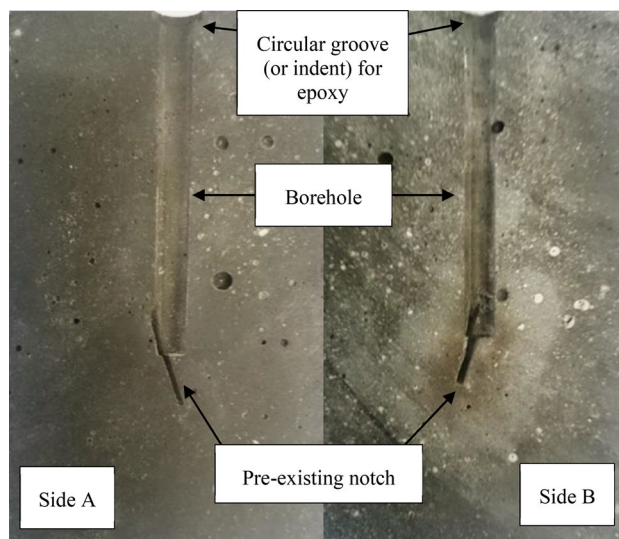


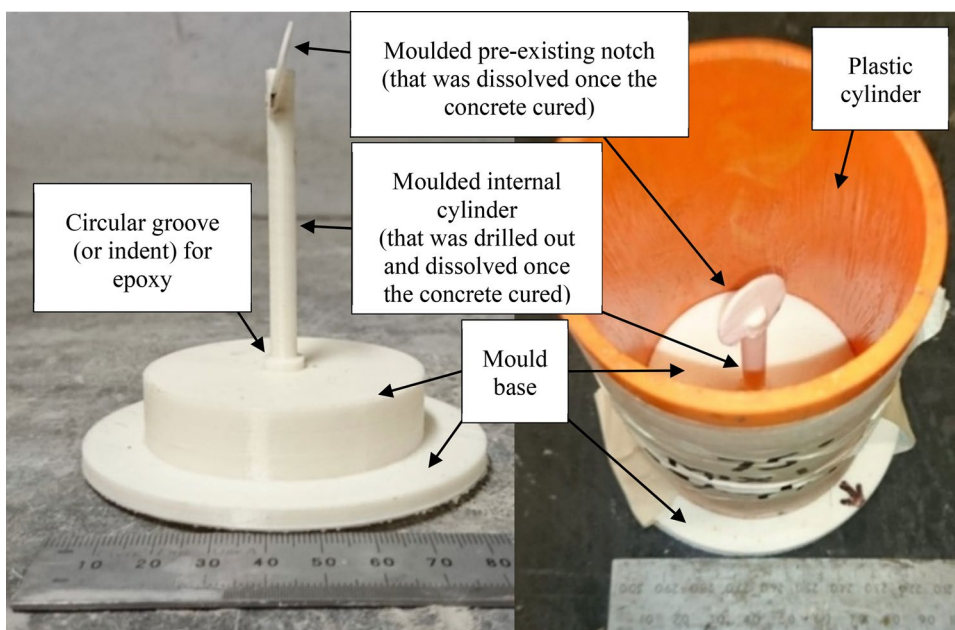
**Fig. 3** Prototype specimen cut in half along the axis of the borehole, showing a 75° pre-existing circular notch at the bottom of the borehole section (on both halves)

for collecting excess epoxy (Sika Anchorfix®-3+) when inserting the injection tube into the borehole.

To measure the mechanical properties of the artificial rocks, two solid blocks were created from two separate mixes using the same mass ratios of base materials (Table 2). The reason of using two separate mixes was to assess the consistency of the mechanical properties. The dimensions of the blocks were 450 mm × 450 mm × 200 mm.

A procedure was adapted from Guo et al. (1993) to produce high strength concrete (see Schwartzkopff et al. (2017)

**Fig. 2** Prototype mould of the 75° pre-existing circular crack



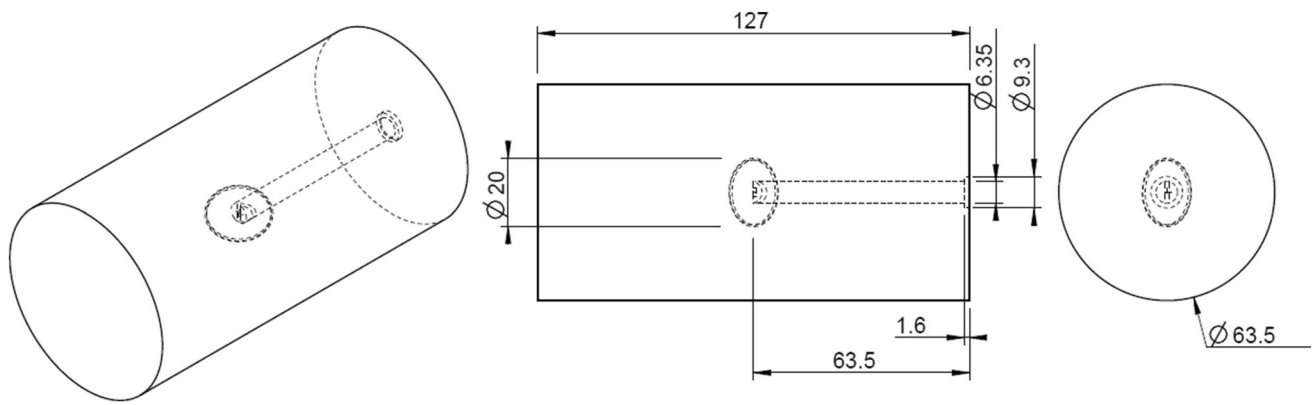


**Fig. 4** Hydraulic fracturing specimen dimensions with a 45° inclined circular crack

for the complete procedure). Note that the specimens for the hydraulic fracturing tests were cast separately. For hydraulic fracturing specimens, the high strength concrete mixture was poured into the specifically designed and manufactured mould (e.g., Fig. 2). The specimens for material property tests were cut out of two blocks using Husqvarna diamond drill with water as the coolant. No impact force was used to cut the specimens to reduce the risk of damaging the specimens before testing. For all specimens, both ends of the specimen were subsequently ground using a diamond wheel on a surface grinder such that both ends are parallel to each other and perpendicular to the axis of the cylindrical specimen.

The deformability properties of the artificial rocks were measured following the method suggested by the International Society of Rock Mechanics (ISRM) (Bieniawski and Bernede 1979). Twelve cylindrical specimens were prepared to measure the Poisson's ratio and elastic modulus, and six of the specimens were taken to the ultimate load to obtain the uniaxial compressive strength (UCS).

The average diameter of these 12 cylindrical specimens was  $63.3 \pm 0.04$  mm and the average height was  $175.0 \pm 0.09$  mm, therefore, the height to diameter ratio was 2.76, between the suggested ratios of 2.5–3.0. Strain gauges were used for the six specimens taken to their ultimate load, and extensometers were used for the other six

specimens. One specimen from each block was used to compare both strain measurement methods and the average difference between these two methods was 0.0014% strain, which was considered negligible. The measured average deformability and mechanical properties of the artificial rock are listed in Table 3. These properties are used in the modelling analyses described later.

The tensile strength was determined from 24 Brazilian disc specimens with an average diameter of  $106.5 \pm 0.03$  mm and a thickness of  $35.0 \pm 0.1$  mm. These specimens were tested until failure occurred. These tests were completed in accordance with the ISRM suggested method (Bieniawski and Hawkes 1978).

Mode I fracture toughness was obtained from 14 tests using cracked chevron notched Brazilian disc (CCNBD) specimens (Fowell et al. 1995). The average thickness of these disks was  $35.0 \pm 0.04$  mm and the average diameter was  $106.4 \pm 0.10$  mm. The maximum half-length of the slot ( $a_1$ ) was  $29.5 \pm 0.07$  mm and the minimum half-length of the slot ( $a_0$ ) was  $12.07 \pm 0.08$  mm.

The material properties of the high strength concrete in Table 3 are similar to those of granite listed in Table 1. A more complete set of material properties for this artificial rock material can be found in Schwartzkopff et al. (2017).

**Table 3** Summary of the artificial rock (concrete) material properties obtained from experiments

Material characteristic	Mean value	Standard error value	Standard error percentage (%)	Number of values
Elastic modulus (GPa)	46.3	1.5	3.2	12
Poisson's ratio	0.22	0.02	7.8	12
Uniaxial compressive strength (MPa)	183.6	3.9	2.1	6
Mode I fracture toughness (MPa $\sqrt{m}$ )	1.18	0.05	3.9	14
Tensile strength (MPa)	6.3	0.7	10.9	24

## 2.2 Hydraulic Fracturing Experiments

To investigate the breakdown pressures and the resultant pressurized crack propagation surfaces, 40 specimens with pre-existing notches were tested. These specimens consist of eight groups with five specimens per group (see Table 4).

Groups 1–3 were hydraulically fractured with no external stresses. The purpose of these tests was to give a reference (baseline) point for the measurement of breakdown pressures and the resultant crack propagation surfaces when no external stresses are applied.

Groups 4–8, with inclined pre-existing notches, were tested under different confining and axial stresses. The confining and axial stresses varied for these experiments to produce a consistent 10 MPa of compressive normal stress on the pre-existing crack plane (when considering an intact specimen) with different shear stresses ranging from 0.5 to 2.5 MPa, in 0.5 MPa increments. The key purpose of this experimental setup was to investigate the influence of the shear stress magnitudes on the breakdown pressure and the resultant crack propagation surfaces. Note that the external stresses are used to define the normal and shear stresses on the crack plane, without considering the stress concentration near the crack front, as outlined in Tada et al. (2000). Therefore, these are only nominal stresses used for calculation purposes. As in reality, these stresses are perturbed by the crack front, as described by the LFM theory. The steps to calculate analytically the stress intensity factors for the initial circular crack are presented in Sect. 3.3. The values of the hydraulic pressure at breakdown are used in Sect. 4.3. The diameter of the initial circular crack was designed to be 20 mm, but the actual value may vary slightly due to the specimen preparation procedure. Therefore, the measured radius was used in the calculation for Mode I stress intensity factor at the breakdown pressure (see Sect. 4.3).

Since an axial load needs to be applied to the specimen and pressurized water needs to be transferred into the centre of the specimen at the location of the circular crack (see Fig. 4 for an example of the specimen), a steel cylinder with an internal conduit system was designed and manufactured. This system allows for the simultaneous application of axial stress and internal hydraulic pressure (see Fig. 5 for the design of the cylinder).

An injection tube was used to transfer the pressurized water into the centre of the specimen. This injection tube has its one end threaded and attached to the internal conduit of the cylinder (Fig. 5). The injection tube was coated in epoxy and then placed into the borehole of the specimen. See Fig. 6a for the dimensions of the injection tube and Fig. 6b for an example of the installation of this component. The injection tube was placed into the borehole of the specimen approximately 14 h prior to testing to allow the epoxy to cure. The use of the injection tube allows

**Table 4** Experiment design, showing the target confining and axial stresses that produce the desired resultant normal and shear stresses on the (inclined) initially circular crack (including the specimen group definitions)

Group	Dip angle (°)	Confining stress (MPa)	Axial stress (MPa)	Normal stress (MPa)	Shear stress (MPa)
1	0	0.00	0.00	0.00	0.00
		0.00	0.00		
		0.00	0.00		
		0.00	0.00		
		0.00	0.00		
2	15	0.00	0.00	0.00	0.00
		0.00	0.00		
		0.00	0.00		
		0.00	0.00		
		0.00	0.00		
3	90	0.00	0.00	0.00	0.00
		0.00	0.00		
		0.00	0.00		
		0.00	0.00		
		0.00	0.00		
4	15	8.13	10.13	10.00	0.50
		10.87	9.71		
		10.50	9.50		
		9.71	10.87		
		10.13	8.13		
5	30	13.73	9.73	10.00	1.00
		11.73	9.42		
		11.00	9.00		
		9.42	11.73		
		9.73	13.73		
6	15	15.60	9.60	10.00	1.50
		12.60	9.13		
		8.50	11.50		
		9.13	12.60		
		10.40	4.40		
7	30	2.54	10.54	10.00	2.00
		6.54	11.15		
		12.00	8.00		
		11.15	6.54		
		10.54	2.54		
8	15	19.33	9.33	10.00	2.50
		14.33	8.56		
		12.50	7.50		
		8.56	14.33		
		9.33	19.33		

water pressure to be transferred to the circular crack without significantly pressurizing the entire borehole section of the specimen to avoid significant deformation of the borehole during the test.

**Fig. 5** A load cylinder with an internal conduit to transfer fluid pressure into the specimen, showing the threads for connecting the external pump line and for attaching the injection tube inserted into the borehole of the specimen

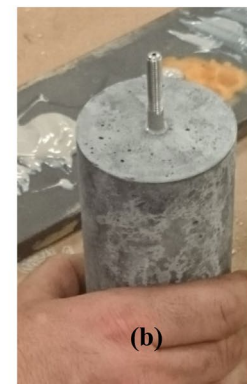
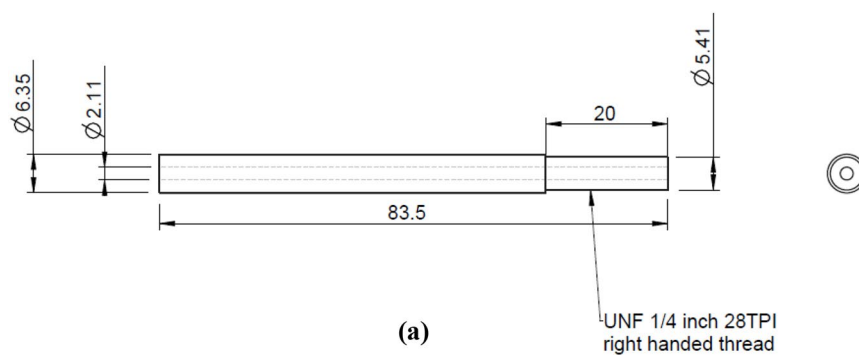
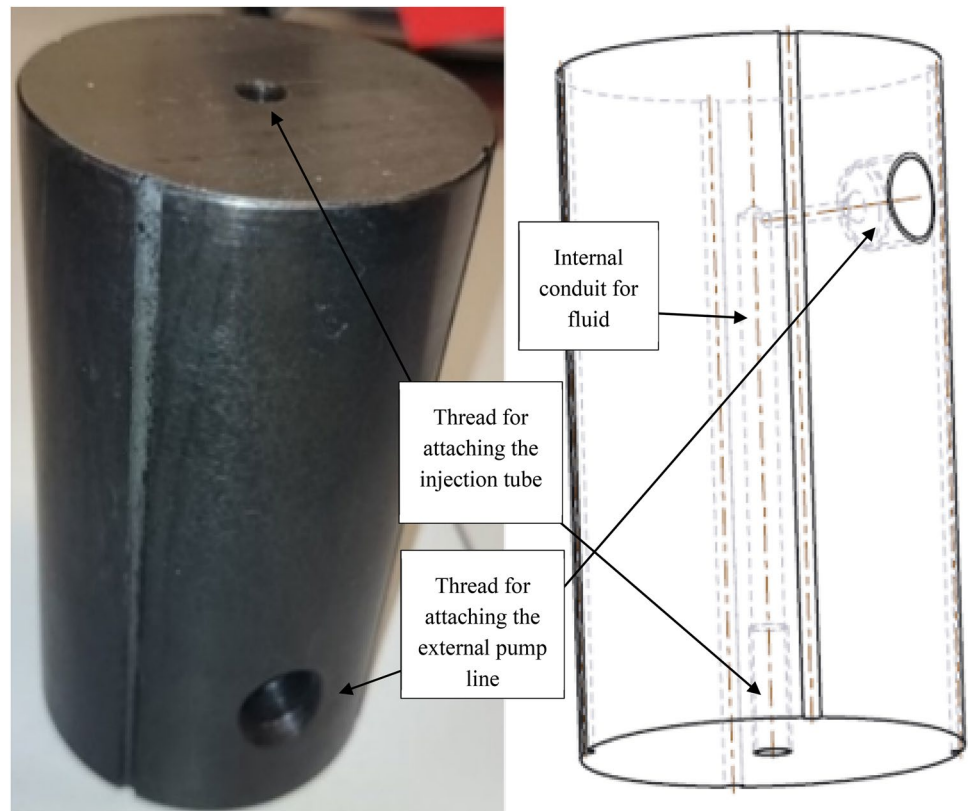


**Fig. 6** **a** Injection tube design and **b** injection tube being placed into the borehole of the specimen

Once the injection tube was in position, the 20 mm of the thread was wrapped in high-density polytetrafluoroethylene (PTFE) thread tape, designed to hold pressures of up to 68.9 MPa. Dental paste was applied to the top surface of the specimen with the injection tube. The load cylinder was then hand screwed onto this injection tube until the faces met before the dental paste hardened. The dental paste sealed the cylinder and the specimen interface and filled any small pores on the surface of the specimen to ensure uniform load transfer (see Fig. 7). Once set, this allows the application of axial stress using a normal

compression loading machine, while the pressurized water can be transferred into the circular crack via the injection tube.

The fluid used for these experiments was a mixture of a water-based black food colouring and distilled water at a volumetric ratio of 1–100, respectively. Henceforth, 40 mL of black food colouring was added to 4 L of distilled water to make the fluid more noticeable if there was a leak and hence to trace the pressurized cracks.

The testing procedure was as follows:



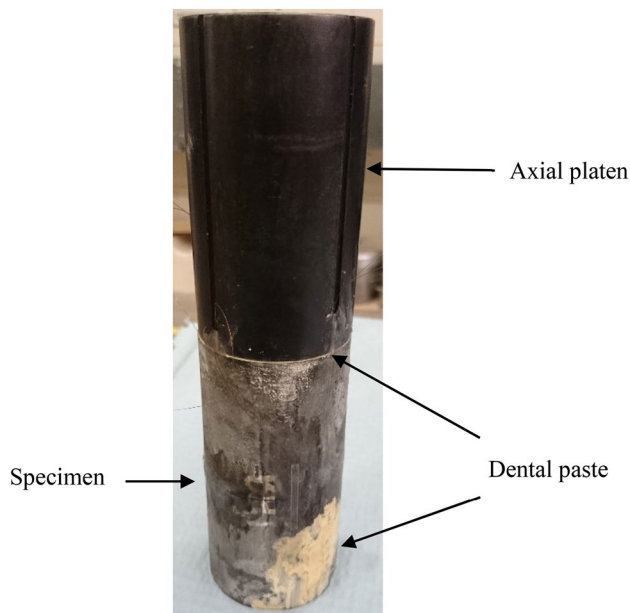


**Fig. 7** The load cylinder attached to a specimen showing the locations of the applied dental paste

1. Using a syringe, the internal cavities inside the load cylinder and the specimen were filled with the coloured water prior to connecting the load cylinder to the syringe pump (Teledyne Isco 65HP High-Pressure Syringe Pump).
2. When connecting the syringe pump line to the load cylinder, the pump was set at a constant flow rate of 1 mL per minute and then hand tightened to reduce the amount of air trapped during the connection process. Once the connection was tightened with a spanner the syringe pump was stopped immediately.
3. A spherical seat was aligned on the top surface of the load cylinder prior to axial loading.
4. The data acquisition server was set to record before the axial load and confining pressures were applied. The axial load was then increased to approximately 1.0 kN. The Hoek cell (see Fig. 8 for its diagram) was hand pumped to 0.5 MPa and then the pressure maintainer was enabled. The loading rate was 0.03 MPa per second to reach the desired stress level within 5–10 min. The axial stress and confining pressure were increased at the same rate until the desired lower value (defined in Table 4) was reached. If the axial stress was larger than the confining pressure, then the Hoek cell pressure maintainer tracked the axial stress until the maximum confining pressure target value was reached. If the confining pressure target was larger than the axial stress target, then approximately 1.0 kN before the maximum load was reached the pressure maintainer was changed to the pre-set rate of 0.03 MPa per second. See Fig. 9 for a

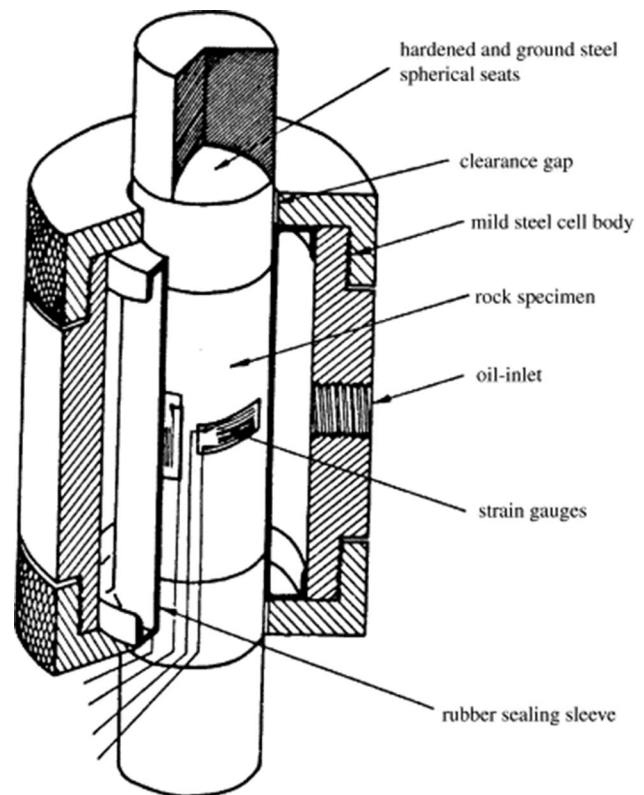


**Fig. 8** Cut away of the Hoek triaxial cell, showing the specimen position and various components of the cell (after Hoek and Franklin 1968)

diagram of these stages and Fig. 10 for the experimental setup.

5. Once the Hoek cell and the axial stress reached their target values, the coloured water was pumped into the specimen at a constant flow rate of 5 mL per minute. This was chosen to produce an average pressurization rate of approximately 1 MPa per second. The pressure and cumulative volume from the syringe pump were recorded during each test, in addition to the external stress conditions.

To use multiple photographs to digitize the resultant propagated crack surface, i.e. using photogrammetry, the specimen had to be split into two parts. This only occurred under reverse faulting stress conditions (where the confining stress is greater than the axial stress), as the high fluid pressure causes a crack to initiate at the notch front and then propagate and realign in a short distance to become approximately horizontal. The specimen did not split into two pieces under normal faulting stress conditions (where the axial stress is greater than the confining stress) since the platens provided enough frictional resistance to inhibit this process from occurring. In this case, the crack initiates

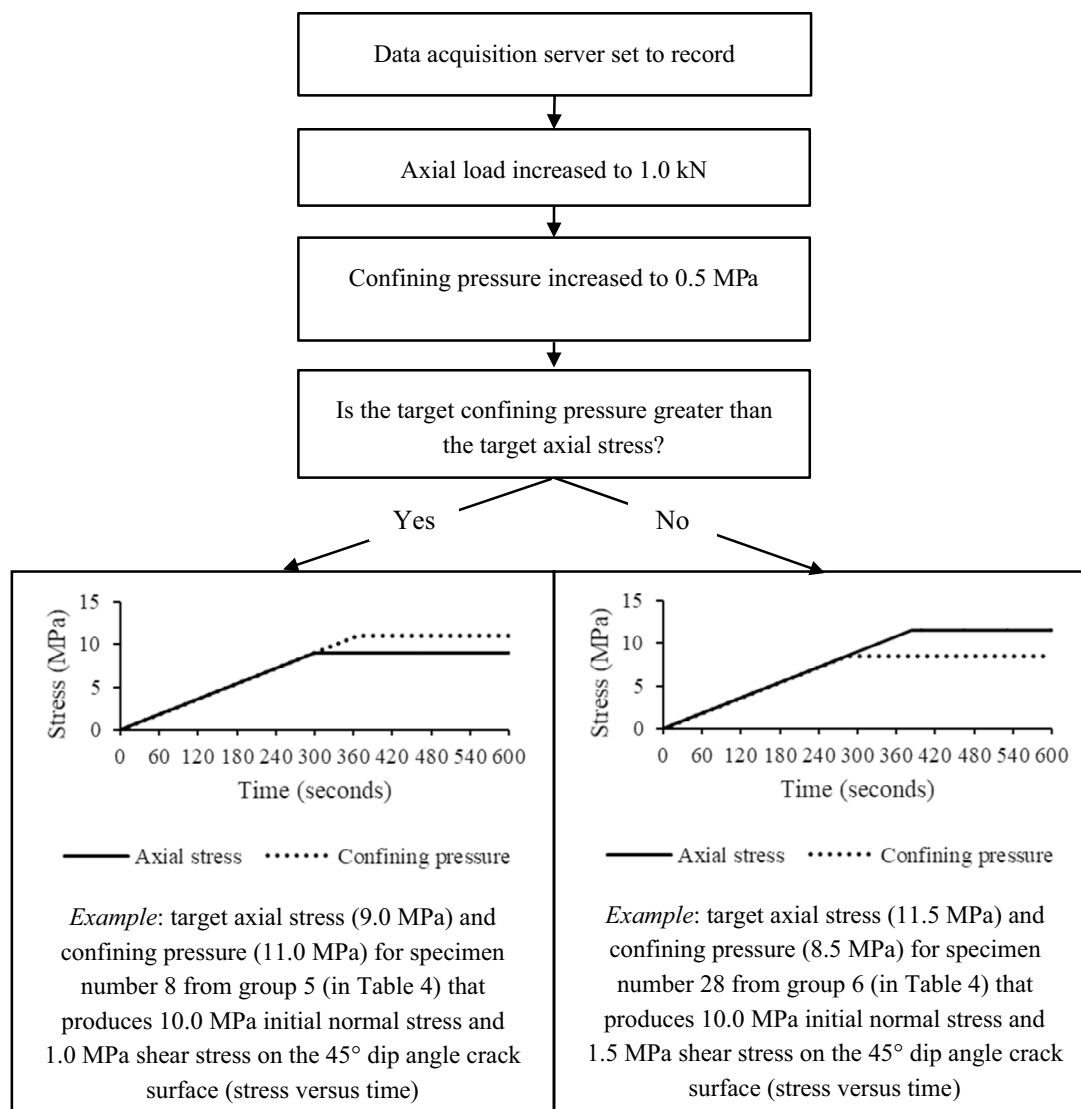


**Fig. 9** Diagram of the detailed loading path before the constant injection flow rate was introduced into the specimen (testing procedure step 4). The axial stress and confining pressure are increased at the same rate initially. If the target confining pressure is greater, then the target axial stress is kept constant when it reaches its target value and

the confining pressure is increased at the same rate until its target is met and then it is held constant. Otherwise, if the target axial stress is greater, then the target confining pressure is kept constant when it reaches its target value and the axial stress is increased at the same rate until its target is met and then it is held constant

from the notch front and then propagates and realigns to be approximately vertical (see Fig. 11 for an example).

For specimens tested under reverse faulting stress conditions and fractured into two halves, the half without the injection tube attached was used to map the crack propagation surfaces. These surfaces were digitized using the ‘Autodesk Memento’ software, subsequently renamed to ‘Autodesk Recap Photo’ software (ReCap|Reality Capture Software|3D Scanning Software|Autodesk 2020). The digitization process requires a maximum of 250 photos taken at different vantage points around the specimen.

In theory, quadrants of the crack propagation surface should be the mirror image of each other, i.e., there are two perpendicular vertical symmetry planes. One plane is along the apex of the circular crack and the axis of the borehole, and the other is perpendicular to this plane and along the axis of the borehole. Once the crack propagation surfaces were digitized, the four surfaces corresponding to the four quadrants were averaged (see Fig. 12 for an example of mapped surfaces of four quadrants). The mean surface thus derived is used for comparison with the numerical analyses.

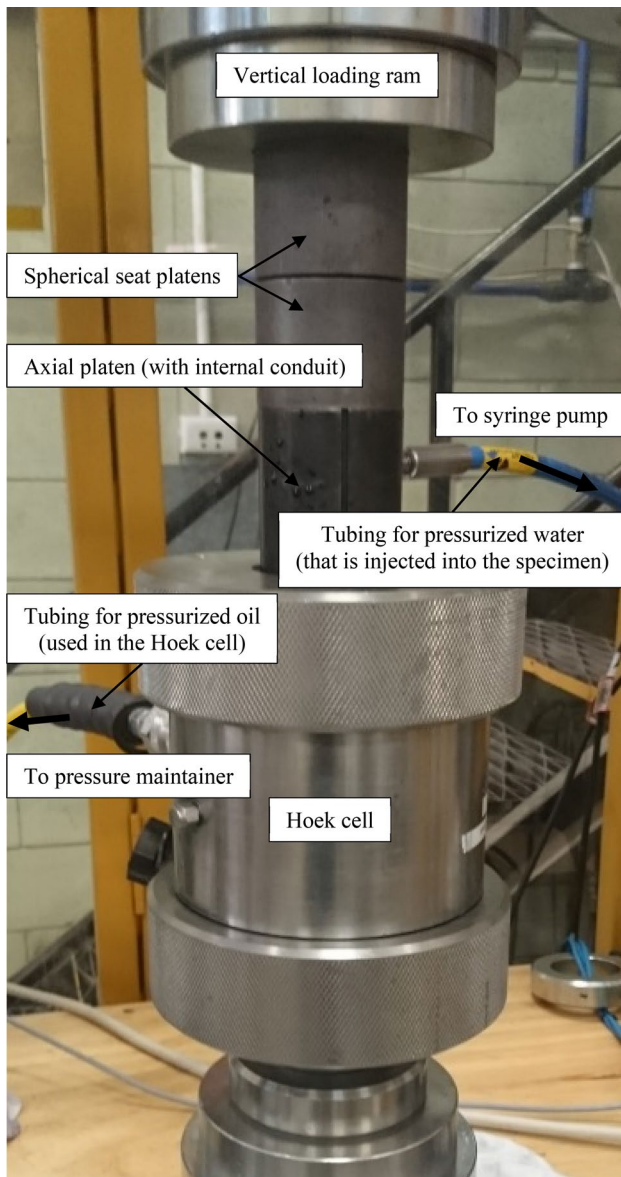


**Fig. 10** Hydraulic fracturing experimental setup. The specimen attached to the load cylinder is located inside the Hoek cell. The spherical seat platens sit on top of the load cylinder and the vertical loading ram applies the axial load to the specimen through the two sets of platens. The tubing from the syringe pump is attached to the load cylinder to inject pressurized water into the specimen. The tubing from the pressure maintainer is attached to the Hoek cell to apply a constant confining pressure to the specimen using pressurized oil

### 3 Theoretical Aspects for the Prediction of the Crack Propagation Surface and Breakdown Pressure of a Pressurized Circular Crack

In the following sections, the analytical procedure to calculate the initial crack propagation step from a circular crack and the numerical method to model the resultant crack

propagation surfaces are discussed. The analysis also gives a method to assess the breakdown pressures for hydraulic fracturing.

#### 3.1 Assumptions Made for the Derivation of the Solution

For the experimental configuration used in this study, it is considered more appropriate to initially apply the elastic stress solutions of a circular (penny shaped) crack in an infinite three-dimensional body than to incorporate the elastic solutions of compressive stresses around a borehole (Kirsch 1898). The borehole is used to transfer the pressurized fluid into the circular crack. The geometry is such that the stresses in the specimen are not significantly perturbed by the borehole. This is due to, in this study, the height of the pressurized borehole section is insignificant compared with the notch radius, the borehole is adhered to the surface of a stainless-steel injection tube, and the initial crack front is sufficiently distant from both the borehole and the boundary of the specimen. These conditions make it suitable to apply the penny shaped crack solutions. Note that if the crack front is too close to the pressurized borehole the stress at the crack front will be perturbed by the presence of the borehole. In this case, the presented analytical solution may become invalid and numerical modelling must be used to evaluate the stress intensity factors. To the best of the authors' knowledge, currently there is no accurate analytical solution for this configuration. The analytical solution presented in this work assumes that the influence of the borehole on the stress field of the specimen is insignificant. In the cases considered, this assumption is acceptable by the numerical cross-validation of the stress intensity factors, which demonstrates insignificant differences between the analytical and the numerical solutions.

In this work, the numerical simulations assumed that the fracturing process could be modelled by LEFM and, therefore, the stress intensity factors calculated by FRANC3D for each quasi-static step can be used to predict the crack propagation surface. The maximum tangential stress criterion was used to calculate this crack front reorientation process. This study demonstrates the effectiveness of using LEFM for the prediction of three-dimensional crack propagation surfaces. A detailed comparison study with other approaches is beyond the scope of this paper. Another assumption used in the numerical modelling is that the internal hydraulic pressure from the previous time step is maintained, i.e. the breakdown pressure is used as the internal pressure at all steps. In addition, the pore pressure change around the crack is considered negligible, which is acceptable as the permeability of the rock-like material used in this study is very low (less than  $9.9 \times 10^{-19} \text{ m}^2$ ) (Schwartzkopff et al. 2017), similar to that of granite. The stable crack propagation distance

**Fig. 11** **a** Diagram of an approximately horizontal crack propagation that occurs under reverse faulting stress conditions, **b** Specimen where the propagating crack broke the specimen in two parts, under reverse faulting stress conditions (i.e. specimen 2 with the crack at dip angle of  $30^\circ$ ; at the breakdown pressure, the normal stress was approximately 10 MPa and shear stress was approximately 0.5 MPa that were produced from an axial stress of 9.72 MPa and a confining stress of 10.91 MPa measured at the instance of breakdown), **c** Diagram of an approximately vertical crack propagation, which occurs under normal faulting stress conditions, **d** Specimen where the propagating crack did not break the specimen into two parts, under normal faulting stress conditions (i.e. specimen 14 with the crack at dip angle of  $60^\circ$ ; at the breakdown pressure, the normal stress was approximately 10 MPa and shear stress was approximately 1.5 MPa that were produced from an axial stress of 12.61 MPa and a confining pressure of 9.16 MPa measured at the instance of breakdown)

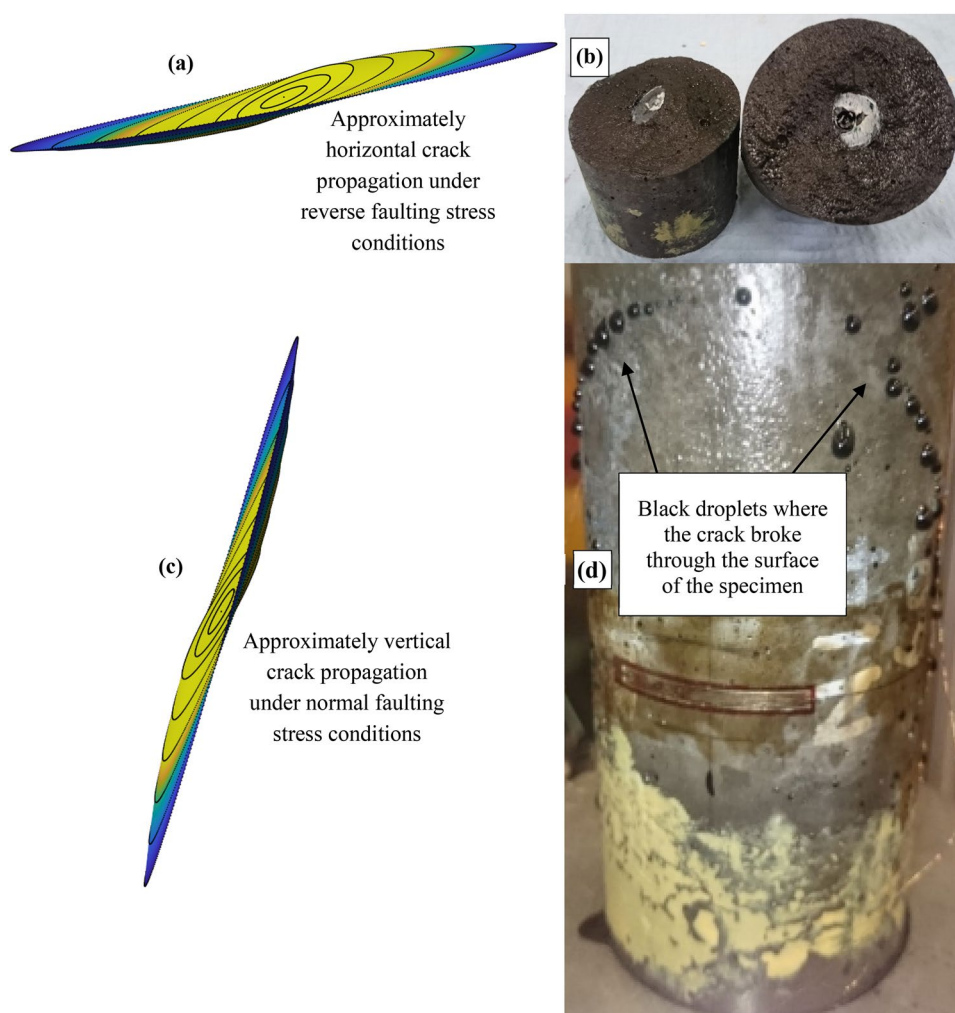
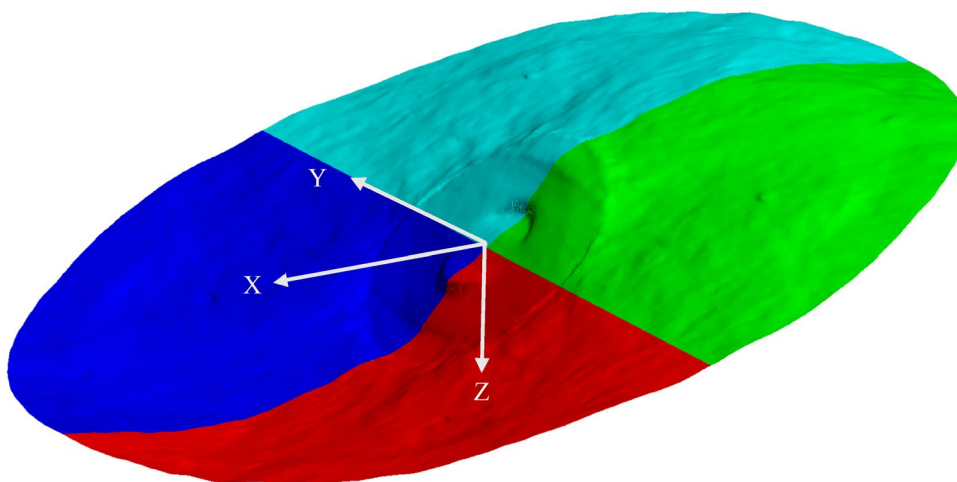


**Fig. 12** Example of mapped surfaces of four quadrants that were then averaged (specimen 23 with the crack at dip angle of  $45^\circ$ . At the breakdown, the confining pressure was 12.52 MPa and the axial stress was 7.50 MPa, corresponding to approximately a normal compressive stress of 10 MPa and shear stress of 2.5 MPa along the crack plane)



could be in the order of millimetres for this material and is most likely related to the critical distance of the material, which is  $5.51 \pm 0.79$  mm (see Schwartzkopff et al. (2017), for this calculation). In reality, once the breakdown pressure is reached the internal fluid pressure is likely to decrease,

depending on the velocity of the crack propagation around the crack front and the injection flow rate. However, since the crack propagation velocity was not known for the experiment it is difficult to extract the critical pressures for each quasi-static propagation step. Therefore, for this study, the

breakdown pressure was used as the internal pressure for all quasi-static crack propagation steps, which is considered reasonable based on the recorded injection pressure profile.

### 3.2 Problem Setup for a Pressurized Circular Crack Subjected to Three Compressive Remote Principal Stresses

Consider a circular crack with a radius  $a$  and oriented with a normal vector  $\bar{\nu}_n$  in a rock block subjected to three compressive remote principal stresses. The crack is internally pressurized by fluid pressure  $P$ . The three principal effective stresses:  $\sigma'_x$ ,  $\sigma'_y$  and  $\sigma'_z$  are oriented along the  $x$ ,  $y$  and  $z$  axes, respectively (Fig. 13). Note that in the case of using a Hoek cell to apply the lateral stress to the cylindrical specimen  $\sigma'_x$  and  $\sigma'_y$  are equal. The influence of the borehole was not considered, since it was in the less significant part (centre) of the crack and its radius (approximately 3.175 mm) was small compared with the radius of the circular crack (approximately 10 mm).

### 3.3 Prediction of the Initial Crack Propagation Front Using the Analytical Stress Intensity Factors for a Pressurized Circular Crack

The following theory provides the details to analyse the stress intensity factors of a circular crack (used to represent the notch in the experiments presented in this study) and the corresponding stress distribution around the crack front. It is assumed that there are no time-dependent effects, i.e. the breakdown pressure is independent of the loading rate. This

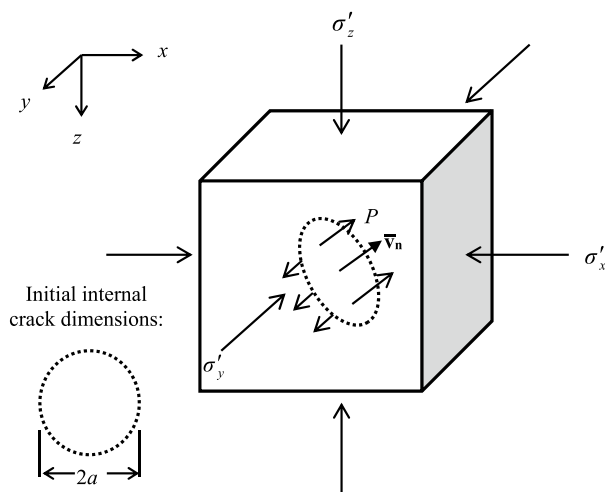


**Fig. 13** Problem formulation showing a circular crack with radius  $a$  and oriented with a normal vector  $\bar{\nu}_n$ , pressurized by fluid pressure  $P$ , inside a material that is subjected to the application of three principal effective stresses:  $\sigma'_x$ ,  $\sigma'_y$ ,  $\sigma'_z$  are oriented along the  $x$ ,  $y$ ,  $z$  axes, respectively

assumption is based on the work of Zoback et al. (1977), which indicated that under constant flow rate experiments (not a constant pressurization rate), there is no time-dependent effect on the breakdown pressure of intact rock.

The pre-existing crack affects the local stress distribution. The stress distribution can be obtained once the stress intensity factors are known. The stress intensity factors can be calculated by the net pressure and the shear stress on the crack face (when considering an intact specimen) due to the external (compressive) stresses. Under the assumption of LEFM, the stress intensity factors can be used to determine the internal pressure when the crack will propagate unstably, and the direction of the crack propagation. The direction of the crack propagation can be determined by the Mode I and Mode II stress intensity factors around the crack front (see Sect. 3.3.2).

It is important to be able to predict the breakdown pressures of a pre-existing crack under different shear stresses, as this will also determine the initial propagation of crack geometry. In general, pre-existing in-situ cracks are subjected to the action of shear stresses due to the unequal regional lateral and vertical stresses.

#### 3.3.1 Stress Intensity Factors for an Internally Pressurized Circular Crack

The stress intensity factors for the considered configuration (see Figs. 13 and 14) can be evaluated using the formulations outlined in Tada et al. (2000). The effective normal stress  $\sigma'_n$  is defined by the compressive normal stress on the crack plane minus the fluid pressure  $P$ . The term net shear stress is defined as the shear stress caused by the unequal external stresses  $\tau$  minus the resisting shear stress  $\tau_r$  on the crack plane. When the crack is closed (i.e. the effective normal stress is greater or equal to zero) the resisting shear stress  $\tau_r$  is  $\mu\sigma'_n$ , where  $\mu$  is the coefficient of friction. However, the defined net shear stress is zero if  $\tau_r > \tau$ . When the crack is open (i.e. when the effective normal stress is less than zero), the resisting shear stress is effectively zero. In the cases presented in this study, at the time of fracturing, the fluid pressure magnitude is greater than compressive normal stress magnitude, therefore, the crack is open and the resisting shear stress  $\tau_r$  is neglected. Note that the shear direction is always parallel to the crack surface by definition, but depending on the remote principal stress magnitudes, this shear direction can be at an angle  $\omega$  from the projected dip direction on the crack plane (Fig. 14). Although, this shear angle  $\omega$  is zero when considering the experimental configuration (i.e. using a Hoek cell where the lateral external principal stress magnitudes are equal but the vertical external principal stress magnitude can be different). The calculations to these variables

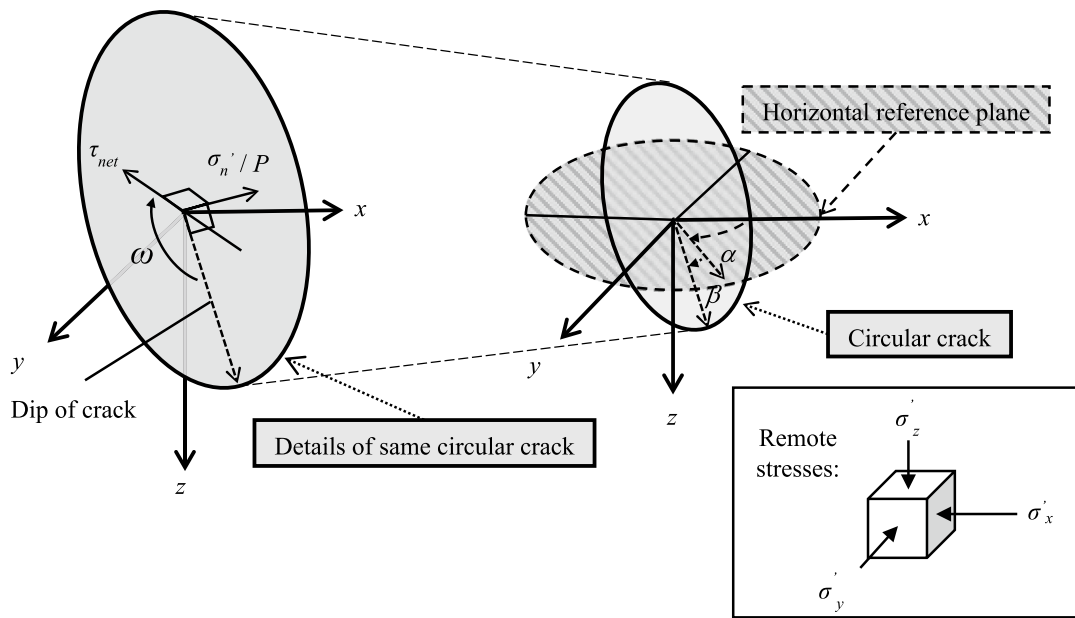


**Fig. 14** The pressurized circular crack illustrating the definitions of the effective normal stress  $\sigma'_n$ , fluid pressure  $P$ , net shear stress  $\tau_{net}$ , shear angle  $\omega$ , dip direction  $\alpha$ , and dip angle  $\beta$ , with reference to the remote stresses

are given below to provide the analytical solution of the stress intensity factors around the circular crack front.

The shear angle  $\omega$  is defined on the crack plane, clockwise around the normal vector in the positive  $z$  axis direction, following the system used in FRANC3D (Wawrzynek et al. 2009). Since Tada et al. (2000) defined the shear angle  $\omega$  clockwise around the negative  $z$  direction, the  $K_{II}(\varphi)$  and  $K_{III}(\varphi)$  values defined by Tada et al. (2000) must be modified accordingly (multiplied by “-1”) to obtain the stress intensity factors consistent to the definitions used in FRANC3D. Using the notations from Rahman et al. (2000), the stress intensity factors can be expressed in the following general forms:

$$\begin{aligned}
 K_I(\varphi) &= -2\sqrt{\frac{a}{\pi}}\sigma'_n \\
 K_{II}(\varphi) &= -\frac{4\cos(\varphi-\omega)}{(2-\nu)}\sqrt{\frac{a}{\pi}}\tau_{net} \\
 K_{III}(\varphi) &= \frac{4(1-\nu)\sin(\varphi-\omega)}{(2-\nu)}\sqrt{\frac{a}{\pi}}\tau_{net}
 \end{aligned} \tag{1}$$

where “-” is used to ensure  $K_I$  is positive for opening crack, to be consistent with the conventional definition and the effective normal stress and net shear stress, as defined above, are calculated along the crack plane of an intact specimen. In other words, the external stresses are used to define the effective normal stress and net shear stress on the crack plane without considering the stress concentration due to the presence of the crack, as outlined in Tada et al. (2000). Therefore, these stresses are only used for calculating the stress intensity factor, as the actual stresses perturbed by

the presence of the crack front, as described by the LEFM theory, will be different.

The normal unit vector  $\bar{v}_n$  of the crack can be calculated from the dip direction  $\alpha$  and dip angle  $\beta$  of the crack plane (see Fig. 14), as shown in Eq. (2). The dip direction here is defined as the clockwise angle around  $z$  (facing downwards) from the positive  $x$  axis.

$$\bar{v}_n = \begin{bmatrix} l \\ m \\ n \end{bmatrix} = \begin{bmatrix} \cos(90^\circ - \beta)\cos(\alpha) \\ \cos(90^\circ - \beta)\sin(\alpha) \\ \sin(\beta - 90^\circ) \end{bmatrix} \tag{2}$$

Young and Budynas (2002) published expressions to calculate the normal and shear stresses on a plane using the normal vector  $(l, m, n)$  for a given external three-dimensional stress configuration. Since it is assumed that  $\sigma'_x, \sigma'_y$  and  $\sigma'_z$  are the effective principal stresses, then  $\tau_{xy}, \tau_{yz}$  and  $\tau_{xz}$  are equal to zero. Therefore, for this system their expressions for normal and shear stresses on a plane can be simplified:

$$\begin{aligned}
 \sigma_{n(\text{external})} &= \sigma'_x l^2 + \sigma'_y m^2 + \sigma'_z n^2 \\
 \tau &= \sqrt{(\sigma'_x l)^2 + (\sigma'_y m)^2 + (\sigma'_z n)^2 - \sigma_{n(\text{external})}^2}
 \end{aligned} \tag{3}$$

where the directional cosines of the shear stress vector are reduced to the following:

$$\begin{bmatrix} l_\tau \\ m_\tau \\ n_\tau \end{bmatrix} = \frac{1}{\tau} \begin{bmatrix} (\sigma'_x - \sigma_{n(\text{external})}) l \\ (\sigma'_y - \sigma_{n(\text{external})}) m \\ (\sigma'_z - \sigma_{n(\text{external})}) n \end{bmatrix} \tag{4}$$

The shear angle  $\omega$  is the angle between the shear direction, Eq. (4), and the vector obtained by projecting the dip direction on the crack plane, i.e.

$$\begin{bmatrix} l_o \\ m_o \\ n_o \end{bmatrix} = \begin{bmatrix} \cos(\beta) \cos(\alpha) \\ \cos(\beta) \sin(\alpha) \\ \sin(\beta) \end{bmatrix}, \tag{5}$$

and can be calculated as:

$$\omega = \arccos \left( \frac{l_\tau l_o + m_\tau m_o + n_\tau n_o}{\sqrt{l_\tau^2 + m_\tau^2 + n_\tau^2} \sqrt{l_o^2 + m_o^2 + n_o^2}} \right) \tag{6}$$

The effective normal stress  $\sigma'_n$  can be calculated as:

$$\sigma'_n = \sigma_{n(\text{external})} - P = (\sigma'_x l^2 + \sigma'_y m^2 + \sigma'_z n^2) - P, \tag{7}$$

where  $P$  is the internal fluid pressure.

Since the resisting shear stress  $\tau_r$ , on the surface of an open crack is essentially zero compared to the shear stress in the material, the net shear stress becomes:

$$\tau_{\text{net}} = \tau - \tau_r = \sqrt{(\sigma'_x l)^2 + (\sigma'_y m)^2 + (\sigma'_z n)^2 - \sigma_{n(\text{external})}^2} \tag{8}$$

Mode I, II and III stress intensity factors are defined by the corresponding stress components (tangential stress  $\sigma_{\theta\theta}$ , radial shear stress  $\tau_{r\theta}$ , and tangential shear stress  $\tau_{t\theta}$ ) multiplied by  $\sqrt{2\pi r}$  as the point of consideration on the plane of the crack front approaches the front of the crack. When evaluating these stress intensity factors, the effective normal stress and the net shear stress defined above must be used. The stress intensity factors calculated from the analytical solution for the configuration studied are very close to those calculated using a numerical model constructed with the help of the commercial software, FRANC3D (Wawrzynek et al. 2009), linked with the FEM code, ABAQUS. The analytical stress intensity factors are used to calculate the first propagation front, and the subsequent stress intensity factors are calculated using the FEM code.

### 3.3.2 Stress Distribution Near an Internally Pressurized Circular Crack and the Initial Prediction of the Crack propagation Front

The formulation of Sih and Liebowitz (1968) on the stress distribution near a circular crack is used to generate the

first quasi-static propagation step by calculating the tangential stress distribution (see Schwartzkopff et al. (2016) for this derivation):

$$\sigma_{\theta\theta} = \frac{\cos^2\left(\frac{\theta}{2}\right)}{\sqrt{2\pi r}} \left[ K_I(\varphi) \cos\left(\frac{\theta}{2}\right) - 3K_{II}(\varphi) \sin\left(\frac{\theta}{2}\right) \right], \tag{9}$$

where the angle  $\theta$  is the crack front angle measured from the radial direction of the crack, clockwise around the tangential vector  $t$ , to the crack front (see Fig. 15 for a diagram showing the crack front angle  $\theta$  and the tangential stress  $\sigma_{\theta\theta}$ ). The maximum tangential stress  $\sigma_{\theta\theta}$  is used to determine the radial crack propagation angles  $\theta_c(\varphi)$  for the first quasi-static propagation step. These radial fracturing angles are calculated from Mode I and Mode II stress intensity factors,  $K_I(\varphi)$  and  $K_{II}(\varphi)$ . The following expression determines the radial crack angles:

$$\theta_c(\varphi) = \begin{cases} 0^\circ & \text{if } K_{II}(\varphi) = 0 \\ 2 \arctan \left[ \frac{K_I(\varphi) \pm \sqrt{K_I(\varphi)^2 + 8K_{II}(\varphi)^2}}{4K_{II}(\varphi)} \right] & \text{if } K_{II}(\varphi) \neq 0 \end{cases} \tag{10}$$

These fracturing angles are evaluated via the following expression:

$$\sigma_{\theta\theta} \sqrt{2\pi r} = \cos^2\left(\frac{\theta_c(\varphi)}{2}\right) \left[ K_I(\varphi) \cos\left(\frac{\theta_c(\varphi)}{2}\right) - 3K_{II}(\varphi) \sin\left(\frac{\theta_c(\varphi)}{2}\right) \right], \tag{11}$$

where the fracturing angle  $\theta_c(\varphi)$  evaluated by Eq. (10) provides the direction of radial crack propagation from a particular point on the crack front to a distance inside the material.

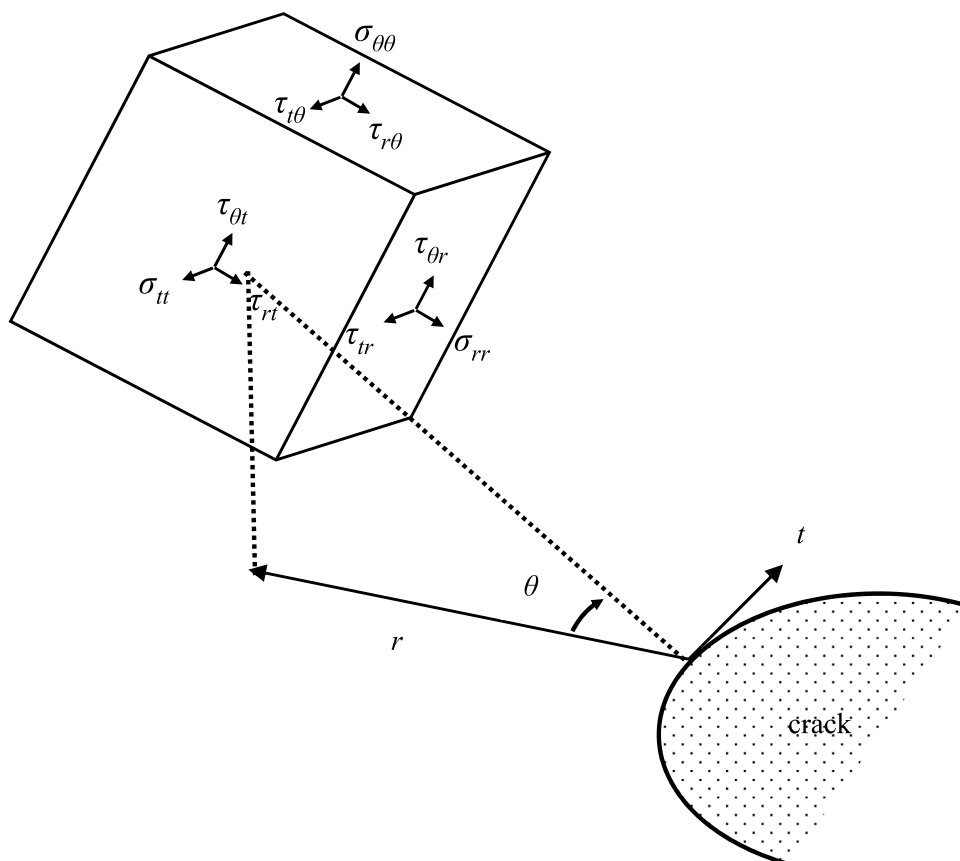
To simplify the analysis, the crack front after the first propagation step was assumed to form a planar polygon. This planar crack front was evaluated and incorporated into FRANC3D during subsequent numerical modelling processes.

### 3.4 Numerical Analysis Using FRANC3D for the Prediction of Subsequent Crack Propagation Surfaces

The commercial software FRANC3D (Wawrzynek et al. 2009) was utilized to model the crack propagation surfaces corresponding to the experiments. The surface was generated by setting the pressure inside the propagating crack to the breakdown pressure.

The same maximum tangential stress criterion was used to determine the crack propagation surface at each quasi-static step. FRANC3D was used in all subsequent steps

**Fig. 15** Stresses on an element near the crack front, showing the cylindrical coordinate system used with radial length  $r$ , tangential direction  $t$ , and rotation angle  $\theta$  from the radial direction



to calculate the stress intensity factors. FRANC3D can be linked with various finite element commercial software packages (ANSYS, NASTRAN, and ABAQUS) where the stresses and displacements are solved (in this work, using ABAQUS). These modelled stresses and displacements around the crack front, are used to evaluate the Mode I, II and III stress intensity factors in FRANC3D with the help of the M-integral method (Wawrzynek et al. 2005).

As discussed in Sect. 3.3.2, the location of the first propagation front was calculated and inserted into the model. This was necessary, as the crack propagation algorithm in FRANC3D is problematic when considering a circular crack. To calculate this planar propagation front, all the radial crack angles at different locations around its circumference were used. The crack increment length  $inc$ , for these steps was set to 20% of the measured initial crack radius, which corresponds to the point of the maximum Mode II stress intensity factor around the front of the crack, which in this case is in the dip direction of the pre-existing circular crack. This increment was approximately the smallest possible increment length that can be used to generate a suitable finite element mesh of a kinked crack. See Fig. 16 for a three-dimensional diagram of the circular crack and subsequent crack front, showing the crack increment length  $inc$  and crack radius  $a$ . The increment

length  $inc$  is measured from the dip of the initial circular crack to the subsequent crack front (see Schwartzkopff et al. (2016) for more details of the calculation of the first crack propagation front).

The increment in subsequent propagation steps was calculated based on the inbuilt FRANC3D propagation algorithm, which is a function of the Mode I stress intensity factor (Paris and Erdogan 1963). This crack propagation algorithm suggests that the higher the Mode I stress intensity factor is at a crack front point, the further this crack point will propagate relative to other points since it has a higher stress concentration. The radial increment  $inc_{\text{FRANC3D}}(\varphi)$ , was therefore determined by the Mode I stress intensity factor  $K_I(\varphi)$ , and the median Mode I stress intensity factor  $K_{I(\text{median})}$ , to the power of a factor  $n$ :

$$inc_{\text{FRANC3D}}(\varphi) = a_{\text{median}} \left( \frac{K_I(\varphi)}{K_{I(\text{median})}} \right)^n. \quad (12)$$

The median increment step size  $a_{\text{median}}$ , was set to 20% of the initial crack radius as discussed above and the factor  $n$ , was set to one (see Fig. 17 for a diagram illustrating the inbuilt FRANC3D propagation algorithm). Note that  $K_{I(\text{median})}$  is not an input parameter but is calculated as the median value of the Mode I stress intensity factors around



**Fig. 16** Three-dimensional diagram of the circular crack and the subsequent crack front, indicating the crack increment length *inc* and crack radius *a* (not to scale), where the increment length *inc* is from the tip of the initial circular crack front to the subsequent crack front

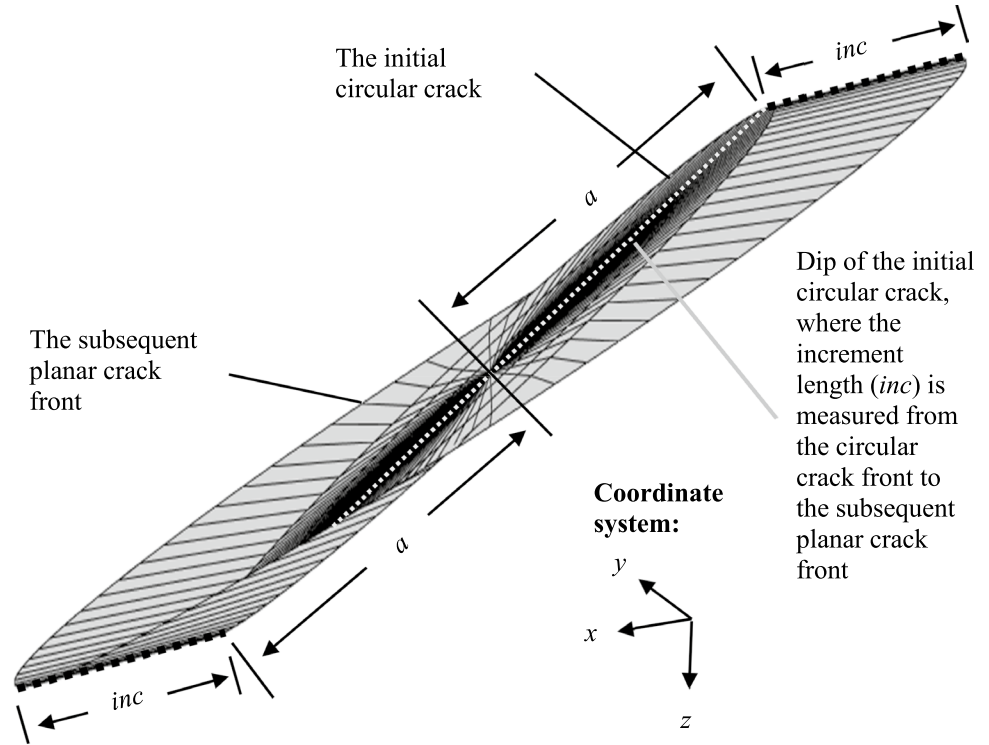
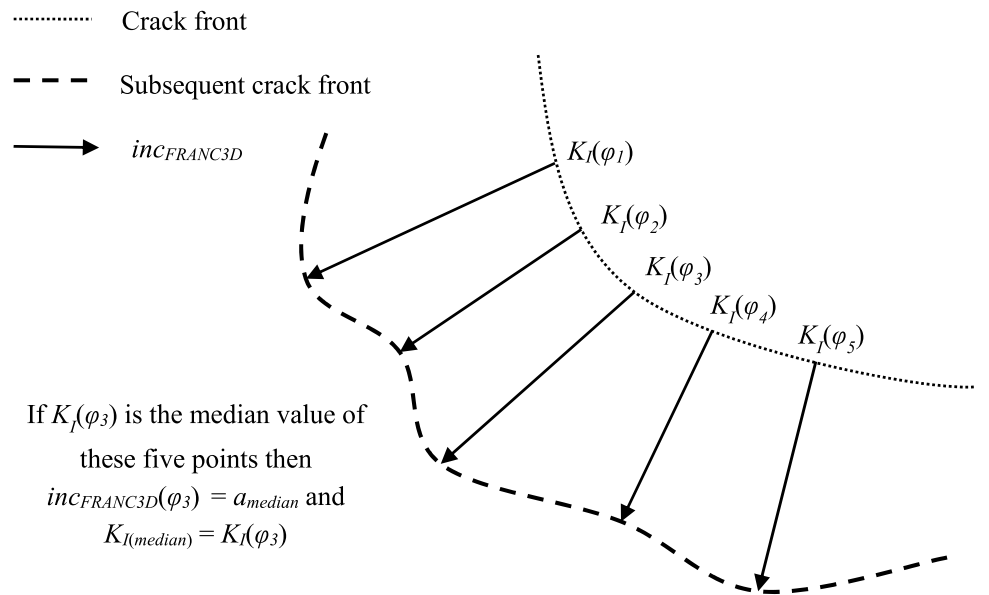


**Fig. 17** Diagram of the inbuilt FRANC3D crack propagation algorithm, illustrating how the length of the subsequent crack propagation front is calculated. The median value of Mode I stress intensity factors is flagged— $K_{I(\text{median})}$ , at this point  $inc_{\text{FRANC3D}}$  equals  $a_{\text{median}}$ , other crack lengths are determined from Eq. (12). Note that the direction of these propagation lengths are determined by the radial direction normal to the tangent of the crack front and the crack fracturing angle given in Eq. (10). When the fracturing angle is non-zero (i.e. the Mode II stress intensity is non-zero), the crack kinks from planar crack propagation



the circumference of the crack front. Therefore, its value will change in each crack propagation step. For  $a_{\text{median}}$ , the model results are not sensitive to the value of this input parameter, but a smaller value is more desirable to generate higher resolution results. Even though  $a_{\text{median}}$  is not a sensitive parameter, it should not be too large as it may cause instability issues commonly encountered in numerical modelling.

FRANC3D, therefore, provided a functioning crack front from its propagation algorithm for the subsequent quasi-static propagation step, even though Mode I stress intensity factors were no longer constant around the front of the kinked crack. By following this method, the crack propagation surface of the specimen tested could be predicted numerically.

## 4 Comparison of Resultant and Predicted Crack Propagation Surfaces and Breakdown Pressures

This section is divided into four parts; in the first part, cross-sections of measured crack propagation surfaces from experiments are described; in the second part, the experimental and numerical crack propagation surfaces for three examples are compared; in the third part, the breakdown pressures for all experiments are analysed; and in the final part, the boundary influence on the breakdown pressures is discussed and analysed.

### 4.1 Crack Propagation Surfaces Obtained from Experiments

Figure 18 provides the cross-sections of the experimental crack propagation surfaces along the dip direction of the circular crack. This illustrates that the greater the shear stress is on the plane of the circular crack, the longer the horizontal section of the resultant crack propagation line will be. The horizontal direction is perpendicular to the minor principal stress direction for these examples. This indicates that, under similar effective normal stress, when the shear stress is greater on the plane of the circular crack the distance will be shorter for the crack to re-orientate to be perpendicular to the minor principal stress direction. Since these examples are under reverse faulting condition, the minor principal stress direction is vertical. A greater shear stress corresponds to a greater difference between the external principal compressive stresses. This trend, of a flatter crack propagation surface when the initial shear stress is higher, is more pronounced in Fig. 18b than in Fig. 18a. In Fig. 18a, specimen 27 with 1.5 MPa of initial shear stress has a similar trend as specimen 22 with 2.5 MPa of initial shear stress. This may be due to the influence of internal fluid pressure at unstable crack propagation (breakdown pressure), as

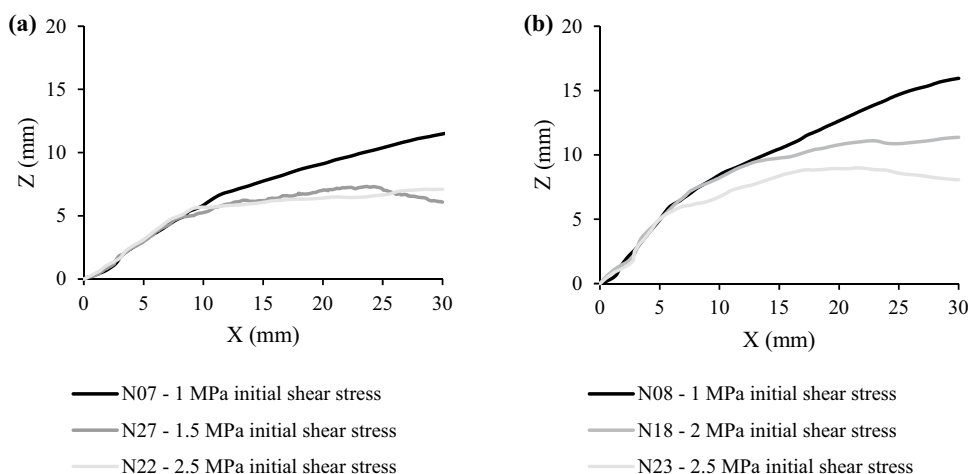
the breakdown pressure for specimen 27 is slightly lower (at 22.43 MPa) compared with that for specimen 22 (at 23.52 MPa). A higher internal fluid pressure with the same shear stress results in a closer to planar crack propagation surface from the initial crack orientation, since the ratio of Mode I to Mode II stress intensity factor is higher. As can be seen from Eq. (10), the greater this ratio is, the less the crack kinks based on the maximum tangential stress criterion. Clearly, from the experiments conducted in this study, the external stress conditions determine the direction of the crack propagation surface and the propagation surface will eventually become horizontal for the reverse faulting stress conditions (where the minor principal stress direction is vertical).

### 4.2 Comparison of Crack Propagation Surfaces from Experiments and Numerical Models

Two sets of crack propagation surfaces are presented below, with each one having three examples. These two sets have two different crack dip angles ( $\beta$ ) of 30° and 45° based on their original circular notches.

These crack propagation surfaces were modelled using FRANC3D as discussed above. The mechanical properties described in Sect. 2.1 were used as inputs for the numerical models. A cuboid model was used, where the length and width of the rectangular prism are equal to the diameter of the circular cross-section of the specimens, i.e. the  $x$  and  $y$  dimensions of the cuboid were 63.5 mm, and the  $z$  dimension was 127 mm. The boundary conditions of these models were fixed to prevent the rotation of the specimen, but without restricting the movement across the faces. Therefore, four corners were pinned in the negative  $z$  direction and likewise in the negative  $x$  and  $y$  directions (see Fig. 19). The boundary effect in these cases (cylindrical or cuboid model) is assumed to be insignificant. As demonstrated by the numerical validation, this assumption is considered

**Fig. 18** Cross-sections of the experimental crack propagation surfaces along the dip direction of the original circular crack, showing a longer horizontal section of the crack propagation line with greater initial shear stress, i.e. the crack realigns to be perpendicular to the minor principal stress direction (the vertical dimension,  $Z$ , is in the direction of the remote minor principal stress): **a** initial dip angle of 30° and **b** initial dip angle of 45°



acceptable for the cases examined (as shown in Sect. 4.4, Table 7 and Fig. 27). In addition, the comparison of the analytical and numerical stress intensity factors indicated that this computational method is valid for the generation of the first crack propagation front.

#### 4.2.1 Crack Propagation Surfaces from a Crack Initially Oriented with a Dip Angle of 30°

The first set of examples for cracks at the dip angle of 30° is summarized in Table 5, where the axial and confining stresses are those obtained from experiments when the breakdown pressure was reached.

The following figures (Figs. 20, 21, 22, 23, 24, 25) show: (a) the specimens after testing with the reference coordinate system used; (b) the mapped experimental crack propagation surfaces; and (c) the modelled crack propagation surfaces. Note that the colour legends for (b) and (c) correspond to the perpendicular distance to the plane of interest. For figures in (b) and (c), the left is the view along the  $z$  axis, the middle is along the  $x$  axis and the right is along the  $y$  axis.

For specimen 7 that had approximately 1 MPa of initial shear stress along the crack plane, the modelled crack propagation surface aligns well with that obtained from the experiment (see Fig. 20 for the comparison). Along the XZ

cross-section the comparison between the modelled and experimental crack lines gives a coefficient of determination ( $R^2$ ) of 0.9957 and a linear regression factor of 0.9755 (calculated based on the differences of the two lines), which are all close to 1 (perfect alignment). The main discrepancy occurs at the outer surface of the specimen, where the crack breaks through causing a sudden drop in the fluid pressure as the crack propagates through the specimen surface. This decrease in the fluid pressure would realign the crack propagation surface more towards being perpendicular to the  $z$  (minor principal stress) direction.

For specimen 27, that had approximately 1.5 MPa of initial shear stress along the crack plane, the modelled and experimental crack propagation surfaces align reasonably well (see Fig. 21 for the comparison), with a  $R^2$  of 0.9860 and a linear regression factor of 1.0778 along the XZ cross-section. In this case, there is a large deviation between the two surfaces at the boundary of the specimen. As discussed above, this may be caused also by the sudden drop in the fluid pressure as the crack propagates through the specimen surface. This decrease in pressure could realign the crack propagation surface more towards being perpendicular to the  $z$  (minor principal stress) direction, as a decrease in the internal fluid pressure reduces the Mode I stress intensity factor while the Mode II stress intensity factor remains approximately unchanged. Therefore, according to the maximum tangential stress criterion, the crack angle increases from straight radial crack propagation (i.e. from 0°) as the ratio of Mode II to Mode I stress intensity factors increases (to a maximum value of approximately 70.5° for pure Mode II loading condition).

For specimen 22, with approximately 2.5 MPa of initial shear stress along the crack plane, the experimental and modelled crack propagation surfaces also align reasonably well (see Fig. 22 for the comparison), with a  $R^2$  of 0.9973 and a linear regression factor of 0.9791 along the XZ cross-section.

#### 4.2.2 Crack Propagation Surfaces from a Crack Initially Oriented with a Dip Angle of 45°

The second set of examples for cracks at a dip angle of 45° is summarized in Table 6.

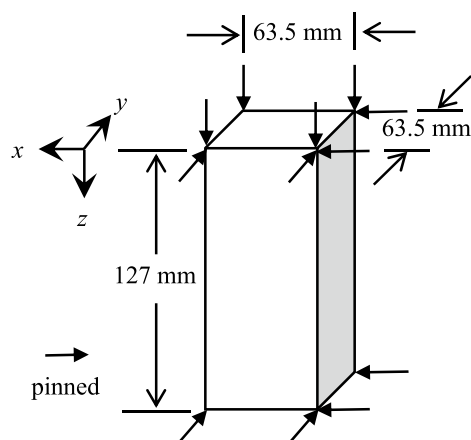
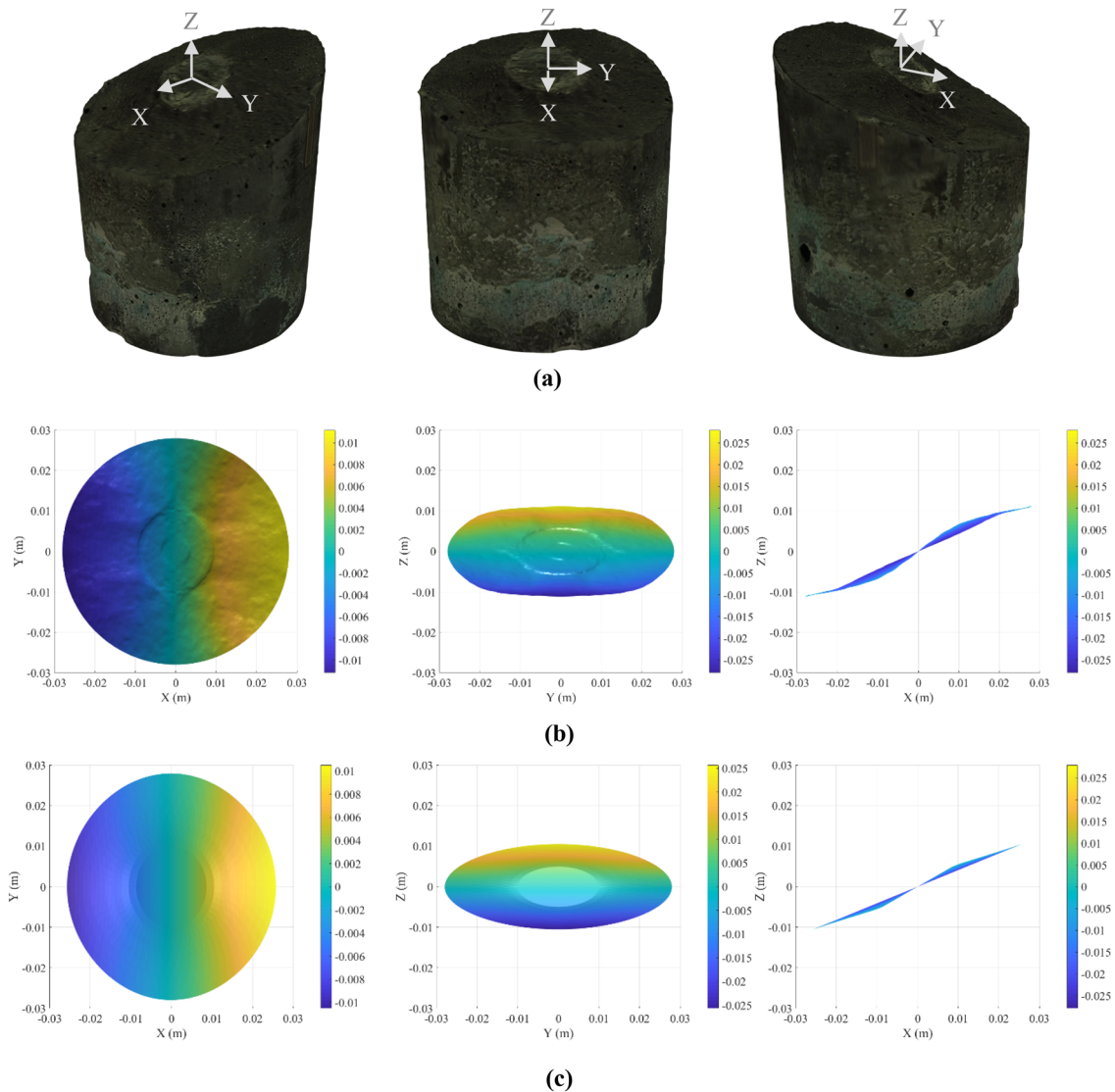


Fig. 19 Numerical model boundary conditions and dimensions

**Table 5** Summary of crack propagation experiments for dip angle of 30°, giving the measured crack radius, confining and axial stresses at breakdown, resultant initial normal and shear stresses on the circular crack and the maximum internal (breakdown) pressure recorded

Specimen number	Dip angle (°)	Crack radius (mm)	Confining pressure (MPa)	Axial stress (MPa)	Normal stress (MPa)	Shear stress (MPa)	Maximum internal pressure (MPa)
7	30	9.96	11.75	9.44	10.02	1.00	24.27
27	30	9.93	12.63	9.13	10.01	1.51	22.43
22	30	9.99	14.38	8.58	10.03	2.51	23.52



**Fig. 20** Comparison of experimental and modelled crack propagation surfaces for specimen 7 showing: **a** The specimen after testing with the reference coordinate system; **b** experimental crack propagation surface; **c** modelled crack propagation surface

The experimental crack propagation surfaces show the same trend discussed above: the greater the shear stress acting on the crack, the shorter the propagation distance before it realigns to be perpendicular to the minor principal stress direction (Figs. 23, 24 and 25). In other words, the higher the shear stress on the initial crack, the flatter the resultant crack propagation surface (for the reverse faulting stress regime). The greater the shear stress on the initial circular crack, the higher the Mode II stress intensity factor and, therefore, according to the maximum tangential stress criterion, the greater the radial angle of the crack propagation will be.

The modelled crack propagation surfaces also show the same discrepancy mentioned above (Figs. 23, 24 and 25), albeit they did not realign to be perpendicular to the minor principal stress direction as much as the crack propagation

surfaces obtained from the experiments. Apart from the boundary and geometry effects mentioned above, there may be other reasons for this slight discrepancy and further analysis of the most likely reasons is required. The discrepancy is, in general, more pronounced for the cracks at the dip angle of  $45^\circ$ , compared with those at the dip angle of  $30^\circ$ .

Figure 23 shows that the two crack propagation surfaces align reasonably well when the shear stress on the crack is approximately 1 MPa, with a  $R^2$  of 0.9979 and a linear regression factor of 1.1311 for the XZ cross-sectional surface profiles.

When the shear stress is approximately 2 MPa, the modelled crack propagation surface follows the same trend as the experimental one (see Fig. 24), with a  $R^2$  of 0.9976 and a linear regression factor of 1.0404 along the XZ plane. The

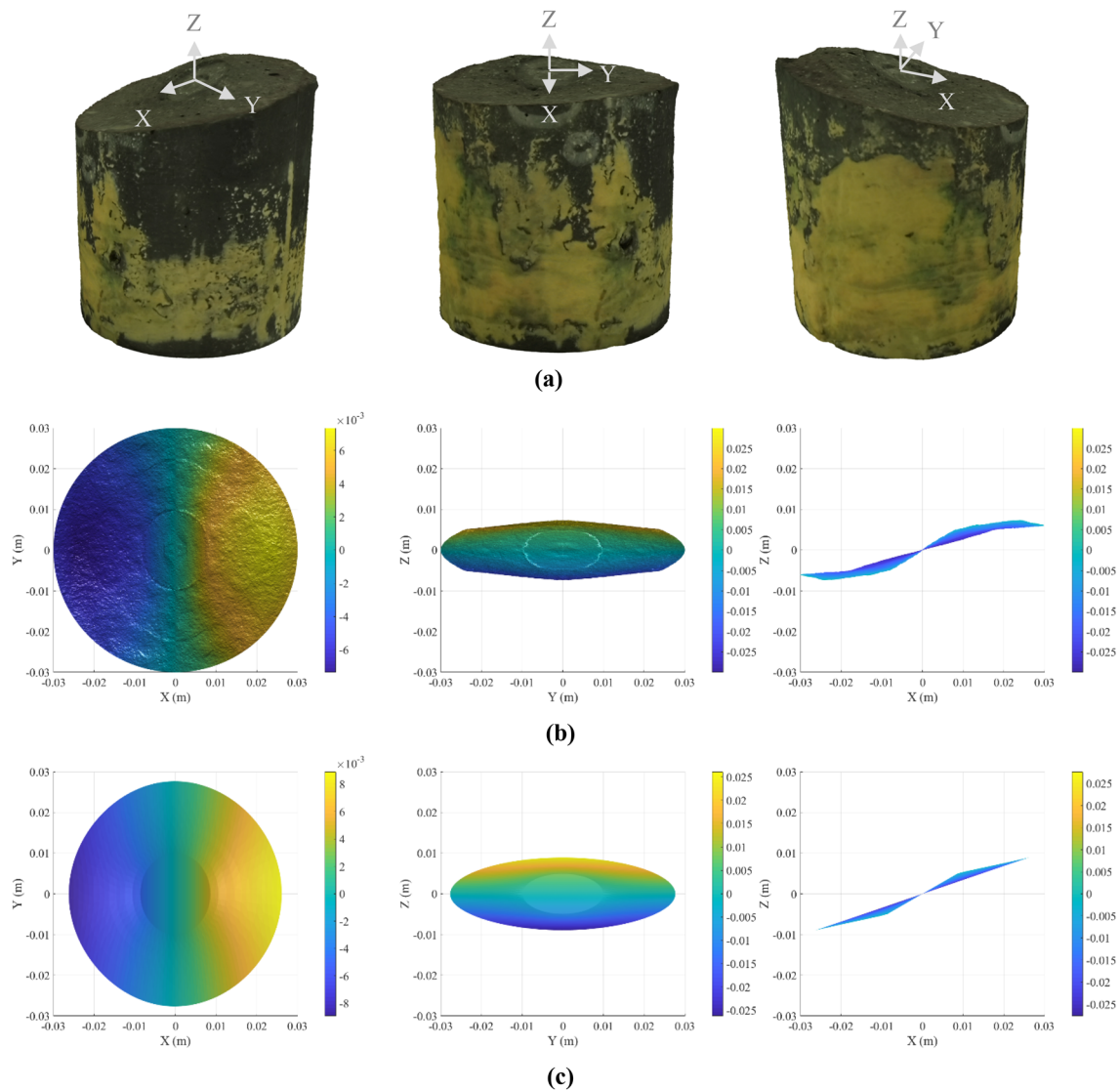


**Fig. 21** Comparison of experimental and modelled crack propagation surfaces for specimen 27 showing: **a** the specimen after testing with the reference coordinate system; **b** experimental crack propagation surface; **c** modelled crack propagation surface

same can also be said when the shear stress is increased to 2.5 MPa (see Fig. 25), with a  $R^2$  of 0.9947 and a linear regression factor of 1.2224 along the XZ plane.

### 4.3 Breakdown Pressures

The effective normal stress and shear stress on the crack plane are converted to Mode I and II stress intensity factors at the time of fracturing for each experimental configuration (see Fig. 26) using Eq. (1). The apparent differences (Fig. 26) in the Mode I stress intensity factor for each set of Mode II stress intensity factor are attributed to the slightly different material properties produced from different batches of concrete (each testing group shown in Table 4 was produced approximately one week apart using the same

procedure given in Sect. 2.2). Therefore, for each group of specimens, which were tested under different shear stress conditions, there were slight variations in conditions and material properties.

The critical Mode I stress intensity factors at the time of fracturing appear to be constant (see Fig. 26) within the range of Mode II stress intensity factors tested. It is expected, however, that the critical Mode I stress intensity factor will gradually decrease with increasing critical Mode II stress intensity factors, as reported in the form of a failure envelope of Mode I versus Mode II critical stress intensity factors for many brittle materials (Ayatollahi et al. 2006; Erdogan and Sih 1963; Sih 1974; Smith et al. 2001). The histogram for the range of measured critical Mode I stress intensity factors have an approximate normal distribution for the cases tested.

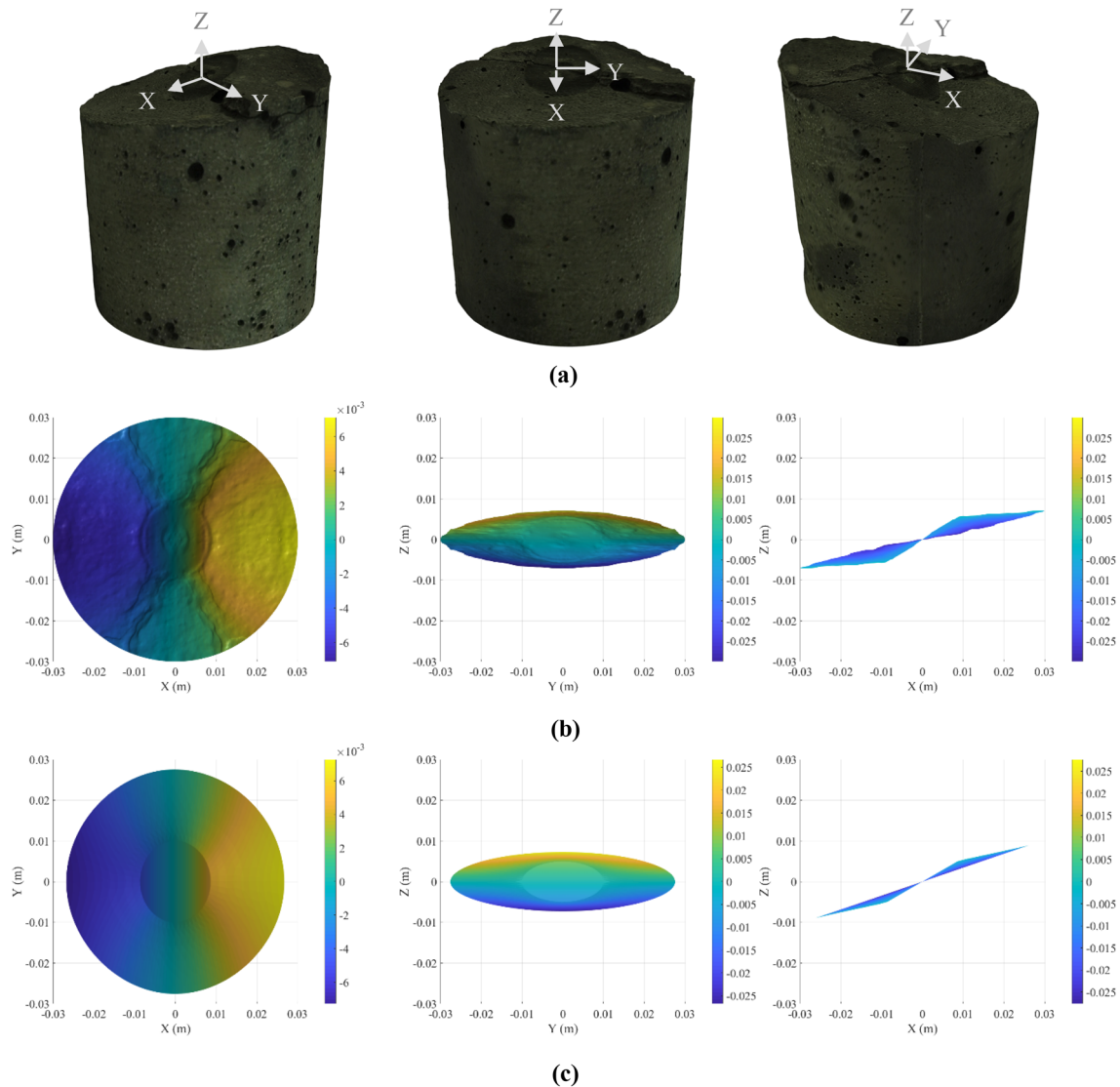


**Fig. 22** Comparison of experimental and modelled crack propagation surfaces for specimen 22 showing: **a** the specimen after testing with the reference coordinate system; **b** experimental crack propagation surface; **c** modelled crack propagation surface

The average critical Mode I stress intensity factor is  $1.24 \pm 0.20 \text{ MPa} \sqrt{\text{m}}$ , calculated from Eq. (1), which was comparable to the Mode I fracture toughness  $K_{Ic}$  value of  $1.18 \pm 0.05 \text{ MPa} \sqrt{\text{m}}$  measured by CCNBD experiments (see Sect. 2.1 and Table 3). The influence of the critical Mode II stress intensity factors on the critical Mode I stress intensity factors, under the shear stress values tested, is not significant in these cases. Therefore, based on the experimental results, the Mode I stress intensity factor of Eq. (1) is used to predict the breakdown pressure  $P_f$ :

$$P_f = \sigma_n + \frac{K_{Ic}}{2} \sqrt{\frac{\pi}{a}}. \quad (13)$$

This expression (Eq. (13)) is derived by setting the Mode I stress intensity factor in Eq. (1) to the fracture toughness  $K_{Ic}$ .

This relationship provides a reasonably accurate estimate of the breakdown pressure values for the experiments conducted in this study. The average predicted breakdown pressure minus the normal stress on the crack ( $P_f - \sigma_n$ ) is predicted to be 10.52 MPa and the corresponding measured average value is 11.08 MPa.

#### 4.4 Boundary Effects on the Breakdown Pressures

The influence of the specimen boundary on the breakdown pressures was investigated using 28 specimens with

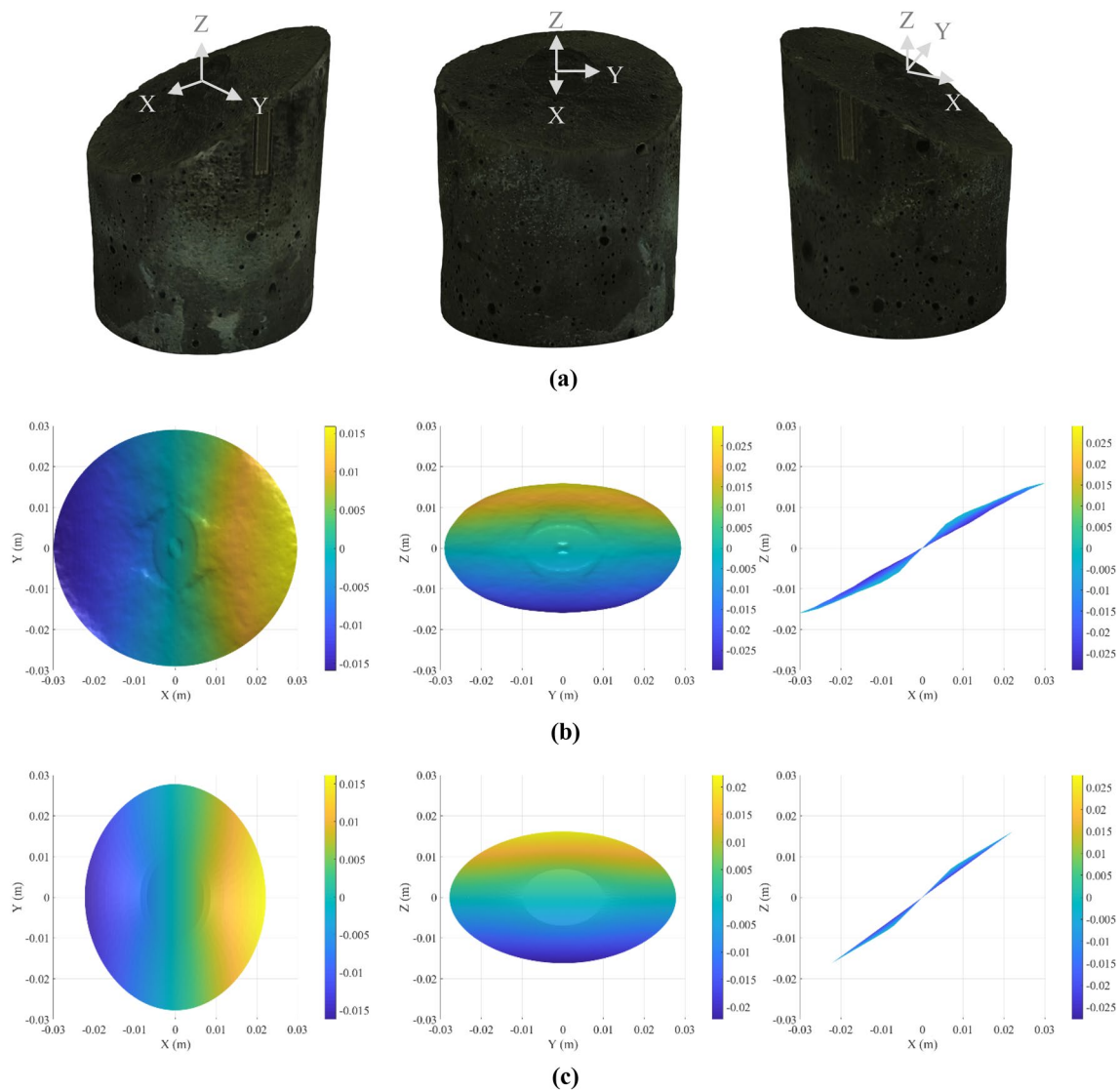


**Fig. 23** Comparison of experimental and modelled crack propagation surfaces for specimen 8 showing: **a** the specimen after testing with the reference coordinate system; **b** experimental crack propagation surface; **c** modelled crack propagation surface

a horizontal notch. The radii of the horizontal notches were manufactured in approximately 5 mm increments, using the same procedure as described in Sect. 2.1, from 5 to 20 mm. Note that specimens with a horizontal notch of 10 mm radius that were used in the experiments described above (Fig. 26) are also included in the analysis in this section.

Again, both the FRANC3D and analytical solutions using the average measured breakdown pressure as the internal pressure are employed to calculate the Mode I stress intensity factors at the breakdown pressure for different cases, and the results are listed in Table 7 and shown in Fig. 27a. The breakdown pressures for these tests are shown in Fig. 27b. The fracture toughness from the CCNBD tests is significantly higher than the Mode I stress intensity factor at the breakdown pressure for the specimens with a crack radius of

15 mm and 20 mm. The fracture toughness is only slightly greater than the Mode I stress intensity factor for the specimens with a crack radius of approximately 5 mm. This suggests that the breakdown pressure prediction (Eq. 13) can only be used when the boundary effect is insignificant, which in this study corresponds to cases when the notch radius is less than 10 mm. As expected, the boundary effects reduce the critical Mode I stress intensity factor at the breakdown to below that of the measured fracture toughness. This is also illustrated by the predicted breakdown pressure (using Eq. (13) with the fracture toughness from CCNBD tests) being significantly higher than the measured breakdown pressures for specimens with a crack radius of 15 mm or 20 mm, as shown in Fig. 27b.

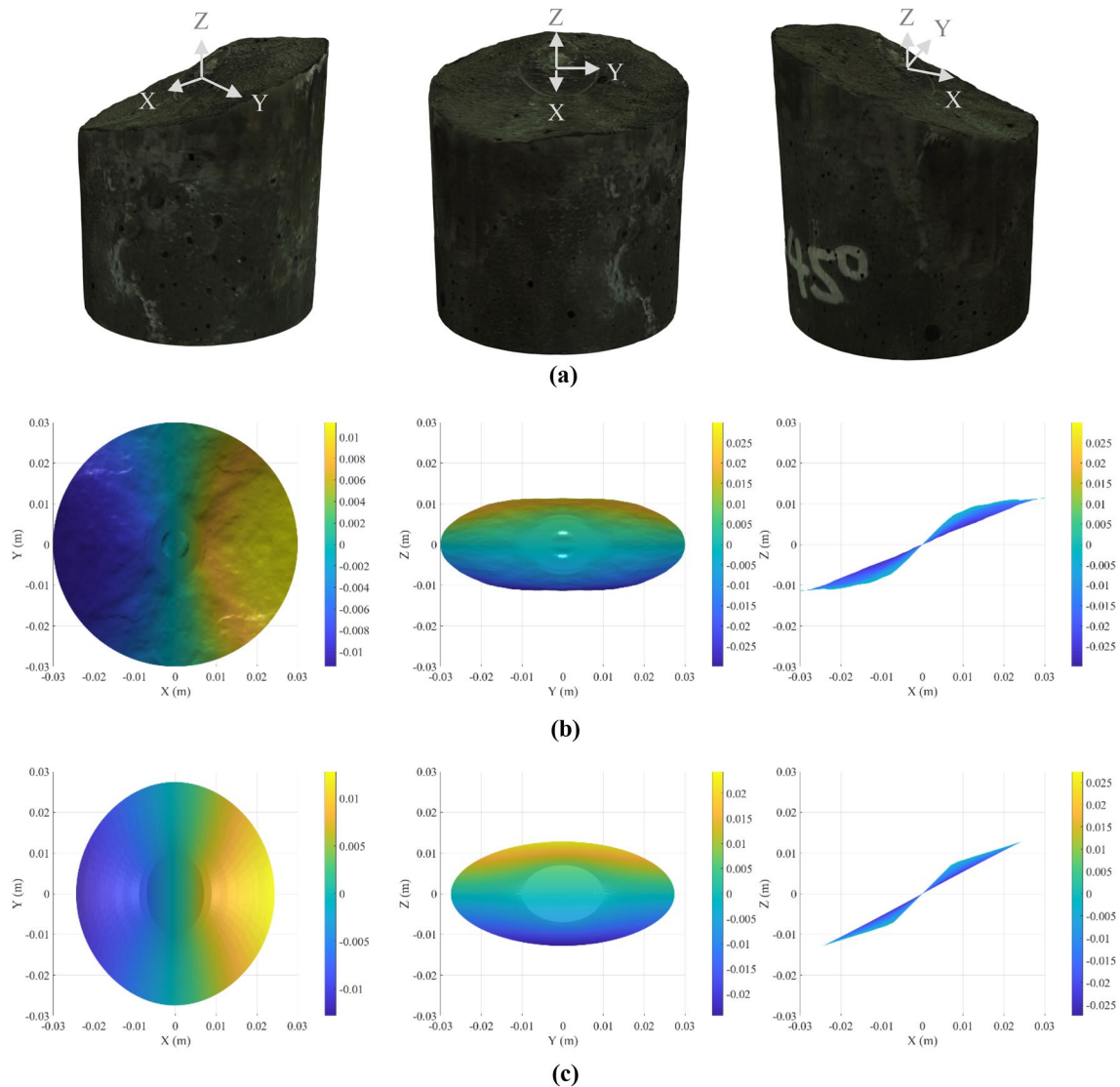


**Fig. 24** Comparison of experimental and modelled crack propagation surfaces for specimen 18 showing: **a** the specimen after testing with the reference coordinate system; **b** experimental crack propagation surface; **c** modelled crack propagation surface

These results further demonstrate the consistency between the analytical and numerical results, even when considering the boundary influence. The results (Table 7 and Fig. 27) also suggest that the boundary influences on the breakdown pressures are significant, as expected, particularly when the original crack front is very close to the specimen boundary. Note that the experiments with the 5 mm radius crack specimens, on average, resulted in lower critical Mode I stress intensity factors compared with that of the 10 mm radius cracks. This is considered to be due to the stress concentration produced by the borehole geometry and the interaction between the borehole and the crack. The 10 mm radius crack specimens have little to no influence from both the borehole and the specimen boundary and, therefore, they were used for most experiments in this study (see previous sections).

## 5 Conclusions

In this research, the effects of circular cracks intersecting a pressurized borehole section on the breakdown pressures and the resultant crack propagation surfaces have been investigated. The results show that, for the hydraulic fracturing configurations studied, the crack propagation surfaces can be approximately modelled, and the associated breakdown pressure can be estimated using the theory of LEFM. For most cases presented, the crack propagation surfaces can be predicted using the proposed crack propagation modelling technique.

Some important findings from this study are summarized below:



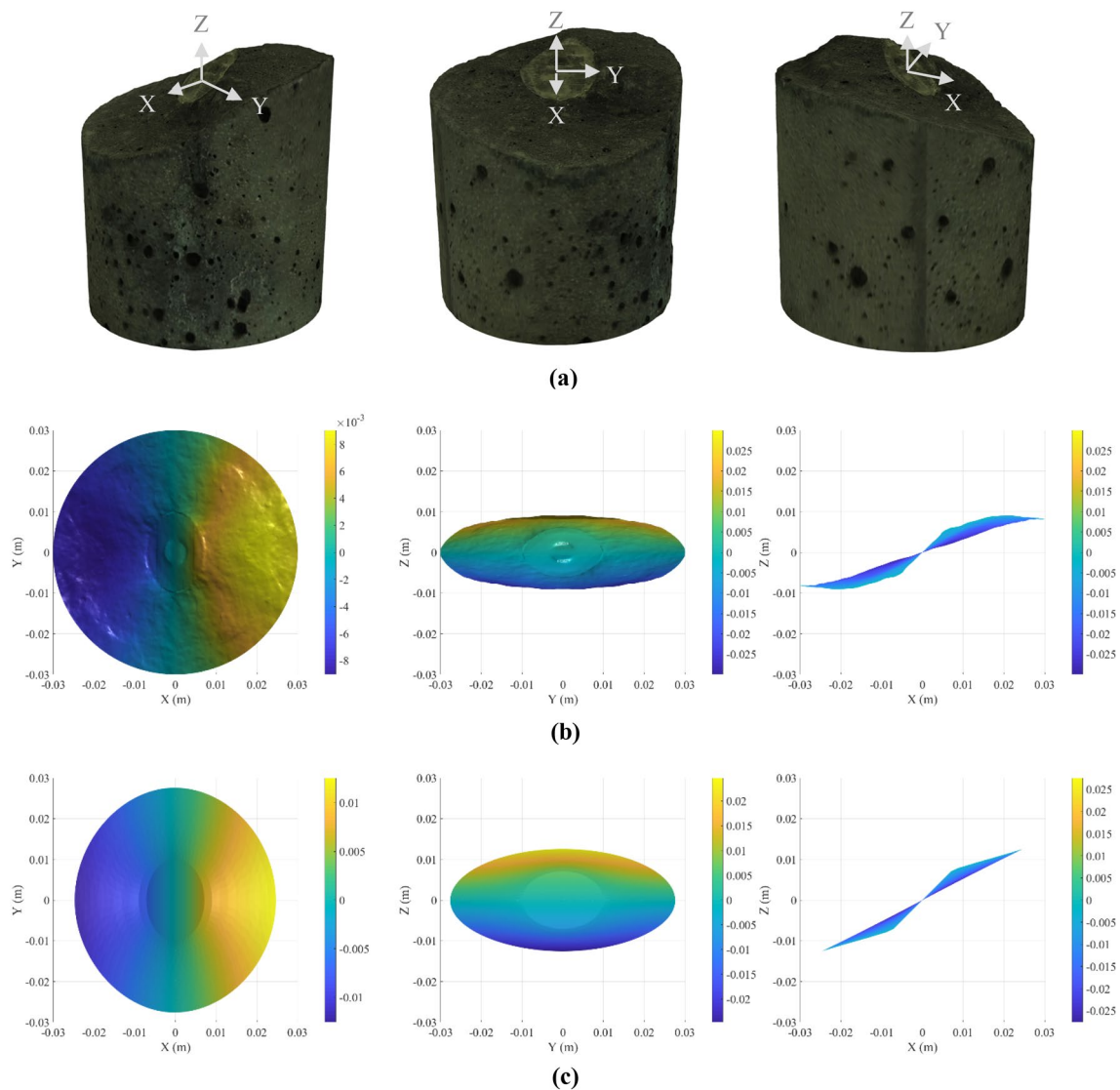


**Fig. 25** Comparison of experimental and modelled crack propagation surfaces for specimen 23 showing: **a** the specimen after testing with the reference coordinate system; **b** experimental crack propagation surface; **c** modelled crack propagation surface

**Table 6** Summary of crack propagation experiments for dip angle of 45°, giving the measured crack radius, confining and axial stresses at breakdown, resultant initial normal and shear stresses on the circular crack and the maximum internal (breakdown) pressure recorded

Specimen number	Dip angle (°)	Crack radius (mm)	Confining pressure (MPa)	Axial stress (MPa)	Normal stress (MPa)	Shear stress (MPa)	Maximum internal pressure (MPa)
8	45	9.90	11.01	9.02	10.02	1.00	22.30
18	45	9.98	12.03	8.04	10.03	1.99	21.86
23	45	10.05	12.52	7.50	10.01	2.51	23.91

- The breakdown pressures of circular notches, designed to replicate a crack, under the shear stress conditions tested, can be reliably predicted by the radius of the crack, the normal stress on the plane of the crack and the fracture toughness of the material, using a LEFM approach.
- The greater the shear stress on the plane of the circular crack, the shorter the distance for the crack to re-orientate

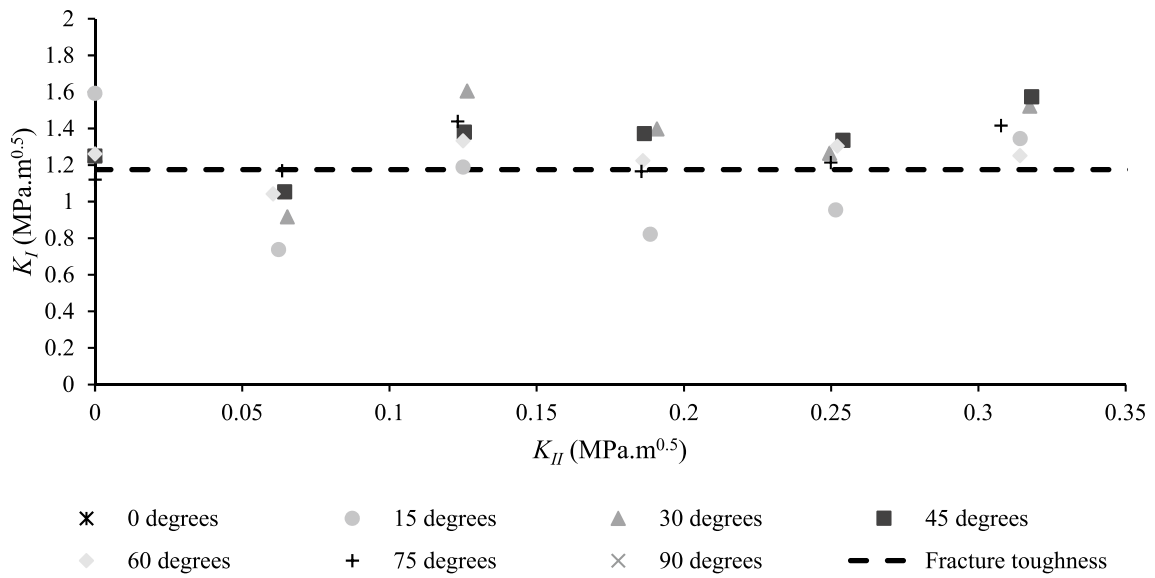


Fig. 26 Critical Mode I versus Mode II stress intensity factors for hydraulic fracturing experiments

Table 7 Comparison of numerical and analytical Mode I stress intensity factors at the average measured breakdown pressures

Average notch radius (mm)	Average maximum internal pressure (MPa)	Standard error (MPa)	Number of tests	Numerical $K_I$ (MPa $\sqrt{m}$ )	Analytical $K_I$ (MPa $\sqrt{m}$ )
5	13.36	0.47	5	1.05	1.05
10	10.99	1.24	10	1.24	1.23
15	1.41	1.35	6	0.20	0.19
20	0.91	0.14	7	0.16	0.14

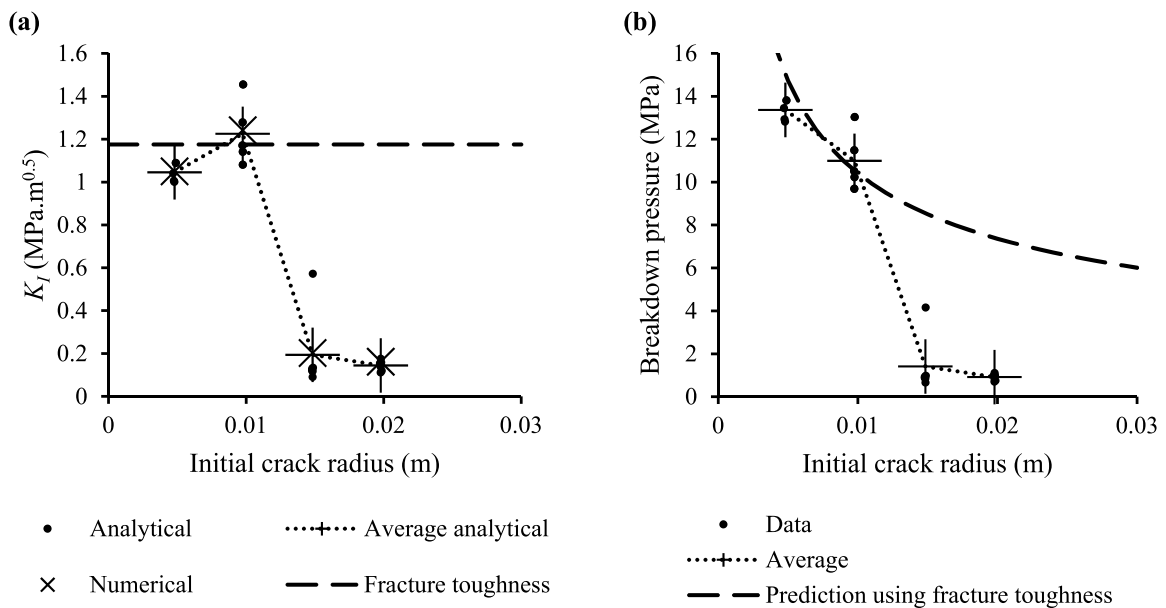


Fig. 27 a Critical Mode I stress intensity factor and b breakdown pressure versus the initial notch radius

to be perpendicular to the minor principal stress direction. The magnitude of the shear stress increases with the increasing difference between the external principal compressive stresses.

- The external stress conditions determine the direction of the crack propagation surfaces. Specifically, the crack propagation plane will eventually realign perpendicular to the minor principal stress direction.
- The boundary effect will become significant when the initial crack front is close to the specimen boundary. The corresponding impact on the breakdown pressure is also significant.
- The material properties of the experimental specimens were well defined and the crack propagation surfaces were mapped in detail. This provides a very useful dataset for future research for the validation of modelling approaches.

Further work is needed to model the variation of the internal pressure versus time during the hydraulic fracturing process. This could then be used to extrapolate the experimental results to larger regions. In addition, as this work only considers the influence of a single circular notch (crack), there is a need to extend the study to cover multiple cracks and their influence on the breakdown pressures and crack propagation surfaces.

**Acknowledgements** The authors would like to thank Adam Rytjes and Simon Golding for their help with the laboratory setup and experiments. In addition, the authors would like to thank Javier Alonso Buitrago Giraldo and Daniel Bowmer for conducting the laboratory experiments to investigate the influence of the specimen boundary on the breakdown pressure of the artificial rock.

## References

- Abass HH, Hedayati S, Meadows D (1996) Nonplanar fracture propagation from a horizontal wellbore: experimental study. *SPE Prod Facil* 11:133–137
- Abbas S, Lecampion B (2013) Initiation and breakdown of an axisymmetric hydraulic fracture transverse to a horizontal wellbore. Paper presented at the Effective and Sustainable Hydraulic Fracturing
- Arzúa J, Alejano LR (2013) Dilation in granite during servo-controlled triaxial strength tests. *Int J Rock Mech Min Sci* 61:43–56. <https://doi.org/10.1016/j.ijrmms.2013.02.007>
- Ayatollahi M, Aliha M, Hassani M (2006) Mixed mode brittle fracture in PMMA—an experimental study using SCB specimens. *Mater Sci Eng, A* 417:348–356
- Backers T, Stephansson O, Rybacki E (2002) Rock fracture toughness testing in Mode II—punch-through shear test. *Int J Rock Mech Min Sci* 39:755–769. [https://doi.org/10.1016/S1365-1609\(02\)00066-7](https://doi.org/10.1016/S1365-1609(02)00066-7)
- Bell FG (2013) *Engineering properties of soils and rocks*. Elsevier, Amsterdam
- Bieniawski Z, Bernede M (1979) Suggested methods for determining the uniaxial compressive strength and deformability of rock materials. *Int J Rock Mech Mining Sci Geomech Abstr* 2:138–140
- Bieniawski ZT, Hawkes I (1978) Suggested methods for determining tensile strength of rock materials. *Int J Rock Mech Mining Sci Geomech Abstr* 15:99–103. [https://doi.org/10.1016/0148-9062\(78\)90003-7](https://doi.org/10.1016/0148-9062(78)90003-7)
- Caineng Z et al (2010) Geological features, major discoveries and unconventional petroleum geology in the global petroleum exploration. *Petrol Explor Dev* 37:129–145. [https://doi.org/10.1016/S1876-3804\(10\)60021-3](https://doi.org/10.1016/S1876-3804(10)60021-3)
- Daneshy A (1973) A study of inclined hydraulic fractures. *Old SPE J* 13:61–68
- Detournay E, Carbonell R (1997) Fracture-mechanics analysis of the breakdown process in minifracture or leakoff test. *Old Prod Facil* 12:195–199
- Erdogan F, Sih GC (1963) On the crack extension in plates under plane loading and transverse Shear. *J Basic Eng* 85:519–525
- Fallahzadeh SH, Rasouli V, Sarmadivaleh M (2015) An investigation of hydraulic fracturing initiation and near-wellbore propagation from perforated boreholes in tight formations. *Rock Mech Rock Eng* 48:573–584. <https://doi.org/10.1007/s00603-014-0595-8>
- Fowell RJ, Hudson JA, Xu C, Chen JF (1995) Suggested method for determining mode I fracture toughness using cracked chevron notched Brazilian disc (CCNBD) specimens. *Int J Rock Mech Mining Sci Geomech Abstr* 1:57–64
- Fridleifsson IB, Freeston DH (1994) Geothermal energy research and development. *Geothermics* 23:175–214. [https://doi.org/10.1016/0375-6505\(94\)90037-X](https://doi.org/10.1016/0375-6505(94)90037-X)
- Fu W, Ames BC, Bungler AP, Savitski AA (2016) Impact of partially cemented and non-persistent natural fractures on hydraulic fracture propagation. *Rock Mech Rock Eng* 49:4519–4526. <https://doi.org/10.1007/s00603-016-1103-0>
- Guo F, Morgenstern NR, Scott JD (1993) An experimental investigation into hydraulic fracture propagation—Part 2. Single well tests. *Int J Rock Mech Mining Sci Geomech Abstr* 30:189–202. [https://doi.org/10.1016/0148-9062\(93\)92723-4](https://doi.org/10.1016/0148-9062(93)92723-4)
- Häring MO, Schanz U, Ladner F, Dyer BC (2008) Characterisation of the Basel 1 enhanced geothermal system. *Geothermics* 37:469–495. <https://doi.org/10.1016/j.geothermics.2008.06.002>
- Hoek E, Franklin JA (1968) A simple triaxial cell for field and laboratory testing of rock. *Trans Inst Min Metall Sect A* 77:A22–26
- Hubbert MK, Willis DG (1957) Mechanics of hydraulic fracturing. *J Am Assoc Petrol Geol* 18:239–257
- Khoei A, Vahab M, Hirmand M (2018) An enriched-FEM technique for numerical simulation of interacting discontinuities in naturally fractured porous media. *Comput Methods Appl Mech Eng* 331:197–231
- Kirsch G (1898) Theory of elasticity and application in strength of materials. *Zeitschrift Vevein Deutscher Ingenieure* 42:797–807
- Lhomme T, Detournay E, Jeffery RG (2005) Effect of fluid compressibility and borehole on the initiation and propagation of a transverse hydraulic fracture. Paper presented at the 11th International Conference on Fracture (ICF11), Torino, Italy, 20–25 March 2005
- Llanos EM, Jeffrey RG, Hillis R, Zhang X (2017) Hydraulic fracture propagation through an orthogonal discontinuity: a laboratory, analytical and numerical study. *Rock Mech Rock Eng* 50:2101–2118. <https://doi.org/10.1007/s00603-017-1213-3>
- Majer EL, Baria R, Stark M, Oates S, Bommer J, Smith B, Asanuma H (2007) Induced seismicity associated with enhanced geothermal systems. *Geothermics* 36:185–222. <https://doi.org/10.1016/j.geothermics.2007.03.003>
- Nasseri MHB, Mohanty B (2008) Fracture toughness anisotropy in granitic rocks. *Int J Rock Mech Min Sci* 45:167–193. <https://doi.org/10.1016/j.ijrmms.2007.04.005>

- Paris P, Erdogan F (1963) A critical analysis of crack propagation laws. *J Basic Eng* 85:528–533
- Rahman MK, Hossain MM, Rahman SS (2000) An analytical method for mixed-mode propagation of pressurized fractures in remotely compressed rocks. *Int J Fract* 103:243–258. <https://doi.org/10.1023/a:1007624315096>
- ReCap | Reality Capture Software | 3D Scanning Software | Autodesk. <https://www.autodesk.com/products/recap/overview>. Accessed 9/4/2020
- Renshaw C, Pollard D (1995) An experimentally verified criterion for propagation across unbounded frictional interfaces in brittle, linear elastic materials. *Int J Rock Mech Mining Sci Geomech Abstr* 3:237–249
- Rogner H-H (1997) An assessment of world hydrocarbon resources. *Annu Rev Energy Env* 22:217–262. <https://doi.org/10.1146/annurev.energy.22.1.217>
- Sarmadivaleh M (2012) Experimental and numerical study of interaction of a pre-existing natural interface and an induced hydraulic fracture. Ph. D. dissertation, Curtin University, Perth, Australia
- Schwartzkopff AK, Xu C, Melkounian NS (2016) Approximation of mixed mode propagation for an internally pressurized circular crack. *Eng Fract Mech* 166:218–233
- Schwartzkopff AK, Melkounian NS, Xu C (2017) Fracture mechanics approximation to predict the breakdown pressure using the theory of critical distances. *Int J Rock Mech Min Sci* 95:48–61. <https://doi.org/10.1016/j.ijrmmms.2017.03.006>
- Sih GC (1974) Strain-energy-density factor applied to mixed mode crack problems. *Int J Fract* 10:305–321
- Sih GC, Liebowitz H (1968) Mathematical theories of brittle fracture. In: Liebowitz H (ed) *Fracture. An advanced treatise*, vol 2. Academic Press Inc., New York, pp 128–151
- Smith DJ, Ayatollahi MR, Pavier MJ (2001) The role of T-stress in brittle fracture for linear elastic materials under mixed-mode loading. *Fatigue Fract Eng Mater Struct* 24:137–150. <https://doi.org/10.1046/j.1460-2695.2001.00377.x>
- Stimpson B (1970) Modelling materials for engineering rock mechanics. *Int J Rock Mech Mining Sci Geomech Abstr* 7:77–121. [https://doi.org/10.1016/0148-9062\(70\)90029-X](https://doi.org/10.1016/0148-9062(70)90029-X)
- Tada H, Paris P, Irwin G (2000) *The stress analysis of cracks handbook*, 3rd edn. ASME Press, New York
- Warpinski N, Teufel L (1987) Influence of geologic discontinuities on hydraulic fracture propagation (includes associated papers 17011 and 17074). *J Petrol Technol* 39:209–220
- Wawrzynek P, Carter B, Banks-Sills L (2005) The M-Integral for computing stress intensity factors in generally anisotropic materials. National Aeronautics and Space Administration, Marshall Space Flight Center
- Wawrzynek P, Carter B, Ingraffea A (2009) Advances in simulation of arbitrary 3D crack growth using FRANC3D NG. In: 12th International Conference on Fracture, Ottawa, 2009
- Weijers L (1995) The near-wellbore geometry of hydraulic fractures initiated from horizontal and deviated wells. Delft University of Technology, Delft
- Xu C (2010) Cracked Brazilian disc for rock fracture toughness testing: theoretical background, numerical calibration and experimental validation. Verlag Dr, Muller
- Xu C, Dowd PA, Tian ZF (2015) A simplified coupled hydro-thermal model for enhanced geothermal systems. *Appl Energy* 140:135–145
- Yan T, Li W, Bi X (2011) An experimental study of fracture initiation mechanisms during hydraulic fracturing. *Pet Sci* 8:87–92. <https://doi.org/10.1007/s12182-011-0119-z>
- Yesiloglu-Gultekin N, Gokceoglu C, Sezer EA (2013) Prediction of uniaxial compressive strength of granitic rocks by various non-linear tools and comparison of their performances. *Int J Rock Mech Min Sci* 62:113–122. <https://doi.org/10.1016/j.ijrmmms.2013.05.005>
- Young WC, Budynas RG (2002) *Roark's formulas for stress and strain*. McGraw-Hill, New York
- Zhang GQ, Chen M (2010) Dynamic fracture propagation in hydraulic re-fracturing. *J Petrol Sci Eng* 70:266–272. <https://doi.org/10.1016/j.petrol.2009.11.019>
- Zhou J, Chen M, Jin Y, Zhang G-q (2008) Analysis of fracture propagation behavior and fracture geometry using a tri-axial fracturing system in naturally fractured reservoirs. *Int J Rock Mech Min Sci* 45:1143–1152. <https://doi.org/10.1016/j.ijrmmms.2008.01.001>
- Zimmermann G, Reinicke A (2010) Hydraulic stimulation of a deep sandstone reservoir to develop an enhanced geothermal system: laboratory and field experiments. *Geothermics* 39:70–77. <https://doi.org/10.1016/j.geothermics.2009.12.003>
- Zoback MD, Rummel F, Jung R, Raleigh CB (1977) Laboratory hydraulic fracturing experiments in intact and pre-fractured rock. *Int J Rock Mech Min Sci* 14:49–58. [https://doi.org/10.1016/0148-9062\(77\)90196-6](https://doi.org/10.1016/0148-9062(77)90196-6)

**Publisher's Note** Springer Nature remains neutral with regard to jurisdictional claims in published maps and institutional affiliations.